

INSTABILITY OF A STALLED ACCRETION SHOCK: EVIDENCE FOR THE ADVECTIVE-ACOUSTIC CYCLE

T. FOGLIZZO AND P. GALLETTI

Service d’Astrophysique, DSM/DAPNIA, UMR AIM CEA-CNRS-Université Paris VII, Saclay, France; foglizzo@cea.fr

AND

L. SCHECK AND H.-TH. JANKA

Max-Planck-Institut für Astrophysik, Garching, Germany

Received 2006 June 26; accepted 2006 September 20

ABSTRACT

We analyze the linear stability of a stalled accretion shock in a perfect gas with a parameterized cooling function $\mathcal{L} \propto \rho^{\beta-\alpha} P^\alpha$. The instability is dominated by the $l = 1$ mode if the shock radius exceeds 2–3 times the accretor radius, depending on the parameters of the cooling function. The growth rate and oscillation period are comparable to those observed in the numerical simulations of Blondin & Mezzacappa. The instability mechanism is analyzed by separately measuring the efficiencies of the purely acoustic cycle and the advective-acoustic cycle. These efficiencies are estimated directly from the eigenspectrum and also through a WKB analysis in the high-frequency limit. Both methods prove that the advective-acoustic cycle is unstable and that the purely acoustic cycle is stable. Extrapolating these results to low frequency leads us to interpret the dominant mode as an advective-acoustic instability, different from the purely acoustic interpretation of Blondin & Mezzacappa. A simplified characterization of the instability is proposed, based on an advective-acoustic cycle between the shock and the radius r_∇ where the velocity gradients of the stationary flow are strongest. The importance of the coupling region in this mechanism calls for a better understanding of the conditions for an efficient advective-acoustic coupling in a decelerated, nonadiabatic flow, in order to extend these results to core-collapse supernovae.

Subject headings: accretion, accretion disks — hydrodynamics — instabilities — shock waves — supernovae: general

1. INTRODUCTION

The recent discovery of a strong $l = 1$ instability of stalled accretion shocks in the context of core-collapse supernovae (Blondin et al. 2003; Scheck et al. 2004; Ohnishi et al. 2006; Burrows et al. 2006) has revived the interest in the fundamental stability properties of accretion shocks. This instability could be a major ingredient in the mechanism of acceleration of neutron stars (Scheck et al. 2004, 2006; Janka et al. 2004). It was also considered as a means to instigate g -mode dipole oscillations of the accreting neutron star (Burrows et al. 2006). While most of these authors recognized the presence of an advective-acoustic cycle similar to the one found by Foglizzo (2002, hereafter F02) in a different context, Blondin & Mezzacappa (2006, hereafter BM06) challenged this interpretation and advocated a purely acoustic mechanism. Understanding the mechanism at work in this instability is a crucial step toward correctly extrapolating its consequences in a more realistic astrophysical situation.

The physics of the advective-acoustic cycle is based on the linear coupling between acoustic and advected perturbations through the flow gradients; both entropy and vorticity perturbations act as source terms for the acoustic wave equation (Foglizzo 2001, hereafter F01; Foglizzo & Galletti 2003). This has been known for decades in the field of jet engines, since the pioneering works of Candel (1972), Howe (1975), Marble & Candel (1977), and Abouseif et al. (1984). In the subsonic flow below the stalled shock, this linear coupling is due to the gradients associated with the convergence of the flow, its deceleration, gravity, and cooling. The interaction between the shock and the flow gradients gives birth to an advective-acoustic cycle in which an advected perturbation generates a pressure feedback, which triggers a new advected perturbation at the shock. Although F02 proved the instability of the advective-acoustic cycle in an accelerated iso-

thermal flow, the fate of such cycles in a cooled decelerated flow is still an open question: can they account for the instability observed in the simulations of BM06?

The first aim of the present study is to clarify the instability mechanism at work, using perturbative techniques. The accretion flow is idealized as a perfect gas passing through a stationary shock and subject to cooling processes schematically described by a cooling function $\mathcal{L} \propto \rho^{\beta-\alpha} P^\alpha$, mimicking in the simplest manner the neutrino cooling in the core-collapse context. It is the first time that a linear approach has been used to understand the mechanism of this nonradial instability in the core-collapse context.

A first step is to confirm that the dominating $l = 1$ mode identified by BM06 in the linear phase of their numerical simulation indeed corresponds to the most unstable eigenmode of the linear problem. Beyond the determination of the eigenspectrum and the validation of numerical simulations, we wish to address the question of the instability mechanism, using techniques similar to F02. These techniques allow for a direct interpretation of the full eigenspectrum in terms of the efficiencies of the acoustic cycle and the advective-acoustic cycle. Alternatively, these efficiencies can also be computed in the WKB approximation. We wish to use both methods in order to check whether the instability is of acoustic or advective-acoustic nature. Understanding the nature of the instability leads us to construct, in a companion paper (Foglizzo et al. 2006), a simple toy model, which can be solved analytically and allows us to reach a fundamental understanding of some of the properties of the instability.

The present paper is organized as follows. The boundary value problem associated with this stalled accretion shock is described in § 2, where we establish the boundary conditions at the shock and compare them to those used by Houck & Chevalier (1992, hereafter HC92) in the different context of supernova fallback.

We determine in § 3 the eigenfrequencies of the flows studied by BM06 and compare them with the linear phase of their numerical simulations. Then we investigate in § 4 the mechanism responsible for this instability using the techniques of F02. The purely acoustic cycle is shown to be stable, and the advective-acoustic cycle is shown to be unstable with respect to $l = 1$ perturbations in the range of validity of our approximations. These results are extrapolated to very low frequency perturbations in § 5. The arguments of BM06 are reconciled with the advective-acoustic interpretation of the instability in § 6. Results are summarized in § 7.

2. FORMULATION OF THE EIGENVALUE PROBLEM

2.1. Description of the Stationary Flow

We consider the radial accretion of a perfect gas with an adiabatic index $\gamma = 4/3$, decelerated through a stationary shock at a radius r_{sh} , accreting on the hard surface of a neutron star of mass M and radius r_* . The self-gravity of the accreting gas is neglected. The cooling function \mathcal{L} is defined as a parameterized function of density ρ and pressure P as in HC92:

$$\mathcal{L} \propto \rho^{\beta-\alpha} P^\alpha, \quad (1)$$

which allows us to mimic the effect of neutrino cooling using the same prescriptions $\alpha = 3/2$ and $\beta = 5/2$ or $\alpha = 6$ and $\beta = 1$ as BM06. Neutrino heating and the associated effect of convection are ignored in the present study.

The equation of continuity, the Euler equation, and the entropy equation defining the stationary flow between the shock and the accretor are written in spherical coordinates as

$$\frac{\partial}{\partial r} (r^2 \rho v) = 0, \quad (2)$$

$$\frac{\partial}{\partial r} \left(\frac{v^2}{2} + \frac{c^2}{\gamma - 1} - \frac{GM}{r} \right) = \frac{\mathcal{L}}{\rho v}, \quad (3)$$

$$\frac{\partial S}{\partial r} = \frac{\mathcal{L}}{Pv}, \quad (4)$$

where S is a dimensionless measure of the entropy defined as the following function of pressure and density, normalized by their values P_{sh} and ρ_{sh} immediately after the shock:

$$S \equiv \frac{1}{\gamma - 1} \log \left[\frac{P}{P_{\text{sh}}} \left(\frac{\rho_{\text{sh}}}{\rho} \right)^\gamma \right]. \quad (5)$$

Note that the pressure force in the Euler equation (3) has been transformed using both this definition of S and the sound speed c defined by $c^2 \equiv \gamma P / \rho$:

$$\frac{\nabla P}{\rho} = \nabla \left(\frac{c^2}{\gamma - 1} \right) - \frac{c^2}{\gamma} \nabla S. \quad (6)$$

The shock is assumed to be adiabatic. Following HC92 and BM06, we assume that the preshock velocity v_1 of the incoming gas is close to free fall, $v_1 \sim v_{\text{ff}} \equiv -(2GM/r_{\text{sh}})^{1/2}$, and that the gas is cold, $\mathcal{M}_1 \gg 1$. The Mach number $\mathcal{M} \equiv |v|/c$ is defined as a positive number.

The assumption of stationarity required by the linear approach introduces a mathematical singularity at the surface r_* of the accretor, where $v(r_*) = 0$; the density diverges according to equa-

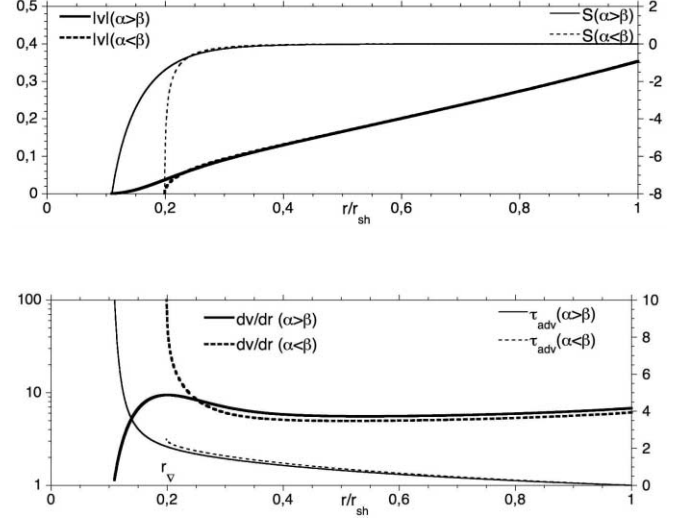


FIG. 1.—Comparison of the stationary flows associated with the cooling parameters $\alpha = 6$ and $\beta = 1$ (solid lines) and $\alpha = 3/2$ and $\beta = 5/2$ (dashed lines). The velocity and entropy profiles (top) are similar in the outer parts of these two flows. The advection time τ_{adv} from the shock to the accretor surface is finite if $\alpha < \beta$ and infinite if $\alpha > \beta$. The velocity gradient reaches a maximum at some intermediate height denoted by $r_{\nabla} > r_*$ if $\alpha > \beta$, whereas $r_{\nabla} = r_*$ if $\alpha < \beta$. The strength of cooling is chosen such that $r_{\text{sh}}/r_{\nabla} = 0.2$ in both flows.

tion (2) and the sound speed decreases to zero. Such pathologies are common in linear studies of cooled accretion on a hard surface (e.g., Chevalier & Imamura 1982; Saxton 2002), whatever the cooling function. For the cooling function considered here, two regimes can be distinguished depending on the sign of $\alpha - \beta$:

1. If $\alpha - \beta < 0$, the cooling efficiency increases as the gas cools down, leading to a cooling runaway. The potential energy is negligible compared to the cooling losses, and the advection time to the accretor surface is finite.

2. If $\alpha - \beta > 0$, the cooling efficiency decreases as the gas cools down. The potential energy is comparable to the cooling losses, and the gas takes an infinite time to reach the surface.

These two regimes are illustrated in Figure 1 for the two sets of cooling parameters used by BM06. The bottom panel shows the velocity gradient of the stationary flow, which can participate to couple vorticity and acoustic perturbations (F02; Foglizzo & Galletti 2003). The velocity gradient reaches a maximum at a radius denoted by r_{∇} . Note that if $\alpha < \beta$, this maximum is reached on the accretor surface ($r_{\nabla} = r_*$). The strength of cooling in Figure 1 was chosen such that $r_{\text{sh}}/r_{\nabla} = 5$ in both flows. As noticed by BM06, the two flows are very similar in their outer parts.

We find it convenient to use the variable $\log \mathcal{M}$ rather than the radius r in order to solve numerically the differential system in the cooling layer near the accretor surface. Integration is stopped just above the accretor surface when the Mach number reaches 10^{-9} .

2.2. Differential System Ruling the Perturbed Flow

The flow is perturbed in three dimensions using spherical coordinates. The complex frequency $\omega \equiv (\omega_r, \omega_i)$ of the perturbations is defined such that its real part ω_r defines the oscillation frequency, and its imaginary part ω_i defines the growth rate. The perturbation of velocity $\delta v_r, \delta v_\theta, \delta v_\varphi$, density $\delta \rho$, sound speed δc , and entropy δS are used to define new perturbative functions f, h , and δK , which enable a compact formulation of

the differential system once projected on spherical harmonics $Y_l^m(\theta, \varphi)$:

$$f \equiv v \delta v_r + \frac{2}{\gamma - 1} c \delta c, \quad (7)$$

$$h \equiv \frac{\delta v_r}{v} + \frac{\delta \rho}{\rho}, \quad (8)$$

$$\delta K \equiv r^2 \mathbf{v} \cdot \nabla \times \delta \mathbf{w} + \frac{l(l+1)c^2}{\gamma} \delta S, \quad (9)$$

where $\delta \mathbf{w} \equiv \nabla \times \delta \mathbf{v}$ is the perturbation of vorticity. The resulting differential system is independent of the azimuthal number m :

$$\frac{\partial f}{\partial r} = \delta \left(\frac{\mathcal{L}}{\rho v} \right) + \frac{i\omega v}{1 - \mathcal{M}^2} \left[h - \frac{f}{c^2} + \left(\gamma - 1 + \frac{1}{\mathcal{M}^2} \right) \frac{\delta S}{\gamma} \right], \quad (10)$$

$$\frac{\partial h}{\partial r} = \frac{i\delta K}{\omega r^2 v} + \frac{i\omega}{v(1 - \mathcal{M}^2)} \left(\frac{\mu^2}{c^2} f - \mathcal{M}^2 h - \delta S \right), \quad (11)$$

$$\frac{\partial \delta S}{\partial r} = \frac{i\omega}{v} \delta S + \delta \left(\frac{\mathcal{L}}{\rho v} \right), \quad (12)$$

$$\frac{\partial \delta K}{\partial r} = \frac{i\omega}{v} \delta K + l(l+1) \delta \left(\frac{\mathcal{L}}{\rho v} \right), \quad (13)$$

where the quantity μ^2 used in equation (11) is defined by

$$\mu^2 \equiv 1 - \frac{l(l+1)c^2}{\omega^2 r^2} (1 - \mathcal{M}^2). \quad (14)$$

The lengthy equations describing how the functions f , h , δS , and δK translate into the classical quantities δv , $\delta \rho$, δP , and the explicit expression of $\delta(\mathcal{L}/\rho v)$ and $\delta(\mathcal{L}/Pv)$ in terms of f , h , and δS are written in Appendix A.

2.3. Boundary Conditions at the Shock

The boundary conditions are established by writing the conservation laws in the frame of the perturbed shock. The derivation of these boundary conditions is shown in detail in Appendix B, since we do not use the special system of spatial coordinates used by HC92. These moving spatial coordinates were introduced in perturbative studies of accretion shocks on white dwarfs (Chevalier & Imamura 1982), such that the shock coordinate remains fixed even when the flow is perturbed. By contrast, our boundary conditions are expressed at the radius r_{sh} of the unperturbed shock as functions of the displacement $\Delta \zeta$ of the shock, associated with its velocity $\Delta v \equiv -i\omega \Delta \zeta$. If the shock is strong [$\mathcal{M}_{\text{sh}}^2 = (\gamma - 1)/2\gamma$] and the incoming gas is in free fall ($v_1 = v_{\text{ff}}$),

$$\frac{f_{\text{sh}}}{c_{\text{sh}}^2} = -\frac{1}{\gamma} \frac{\Delta v}{v_{\text{sh}}} - \Delta \zeta \frac{\nabla S_{\text{sh}}}{\gamma}, \quad (15)$$

$$h_{\text{sh}} = \frac{2}{\gamma + 1} \frac{\Delta v}{v_{\text{sh}}}, \quad (16)$$

$$\delta S_{\text{sh}} = -\Delta \zeta \left(\nabla S_{\text{sh}} + \frac{1}{2r_{\text{sh}}} \frac{5 - 3\gamma}{\gamma - 1} \right) - \frac{2}{\gamma + 1} \frac{\Delta v}{v_{\text{sh}}}, \quad (17)$$

$$\delta K_{\text{sh}} = -l(l+1) \Delta \zeta \frac{c_{\text{sh}}^2}{\gamma} \nabla S_{\text{sh}}. \quad (18)$$

These conditions can be translated into the classical quantities δv_r , $\delta \rho$, and δP :

$$\left(\frac{\delta v_r}{v} \right)_{\text{sh}} = \frac{2}{\gamma + 1} \frac{\Delta v}{v_{\text{sh}}} - \frac{2\Delta \zeta}{\gamma + 1} \left[(\gamma - 1) \nabla S_{\text{sh}} + \frac{\gamma}{2r_{\text{sh}}} \frac{5 - 3\gamma}{\gamma - 1} \right], \quad (19)$$

$$\left(\frac{\delta \rho}{\rho} \right)_{\text{sh}} = \frac{2\Delta \zeta}{\gamma + 1} \left[(\gamma - 1) \nabla S_{\text{sh}} + \frac{\gamma}{2r_{\text{sh}}} \frac{5 - 3\gamma}{\gamma - 1} \right], \quad (20)$$

$$\left(\frac{\delta P}{P} \right)_{\text{sh}} = -2 \frac{\gamma - 1}{\gamma + 1} \frac{\Delta v}{v_{\text{sh}}} + \frac{\Delta \zeta}{\gamma + 1} \left[(\gamma - 1)^2 \nabla S_{\text{sh}} + \frac{1 + \gamma^2}{2r_{\text{sh}}} \frac{5 - 3\gamma}{\gamma - 1} \right]. \quad (21)$$

The transverse components δv_θ and δv_φ of the velocity perturbation after the shock are related to the nonspherical deformation of the shock through

$$(\delta v_\theta)_{\text{sh}} = \frac{v_1 - v_{\text{sh}}}{r_{\text{sh}}} \frac{\partial \Delta \zeta}{\partial \theta}, \quad (22)$$

$$(\delta v_\varphi)_{\text{sh}} = \frac{v_1 - v_{\text{sh}}}{r_{\text{sh}} \sin \theta} \frac{\partial \Delta \zeta}{\partial \varphi}. \quad (23)$$

The divergence of the transverse velocity can be projected on the spherical harmonics Y_l^m and satisfies the following boundary condition for a strong shock:

$$\frac{r_{\text{sh}}}{\sin \theta} \left[\frac{\partial}{\partial \theta} (\sin \theta \delta v_\theta) + \frac{\partial}{\partial \varphi} \delta v_\varphi \right] = -\frac{2l(l+1)}{\gamma - 1} v_{\text{sh}} \Delta \zeta. \quad (24)$$

Equations (19), (20), and (21) are in perfect agreement with equations (50), (52), and (53) of HC92, which can be recovered by taking into account the gradients of the stationary flow quantities v , ρ , and P , using a Taylor expansion between r_{sh} and $r_{\text{sh}} + \Delta \zeta$.

Transverse velocities at the shock are precluded by equation (51) of HC92, in contradiction with our equations (22), (23), and (24) and also with other linear studies involving transverse perturbations such as Bertschinger (1986), Imamura et al. (1996), or Saxton & Wu (1999). As a consequence, the stability results reported by HC92 for nonradial perturbations should be considered as questionable, while their results concerning radial perturbations should be unaffected.

3. NUMERICAL DETERMINATION OF THE EIGENFREQUENCIES

3.1. Numerical Method

The differential system is solved by integrating over the variable $\log \mathcal{M}$ from the shock down to the accretor surface, at a point where $\mathcal{M} = 10^{-9}$ if the advection time is finite ($\alpha < \beta$). As an illustration, the radial shape of the eigenfunctions associated with the most unstable $l = 1$ mode in the flow with $\alpha = 3/2$, $\beta = 5/2$, and $r_{\text{sh}}/r_* = 10$ is shown in Figure 2 (*top*). Using $\log \mathcal{M}$ as a variable allows us to compute the eigenfunctions down to the singular accretor surface. Structures are visible down to $\mathcal{M} \sim 10^{-4}$, corresponding to radial scales, which are much too small to be accessible to existing numerical simulations ($< 10^{-9} r_{\text{sh}}$). Luckily, these scales do not need to be resolved to measure the correct eigenfrequency, as shown in Figure 2 (*bottom*). Varying the depth r_{bc} at which the boundary condition $\delta v(r_{\text{bc}}) = 0$ is applied indicates that the regions of the flow where $\mathcal{M} < 4 \times 10^{-3}$

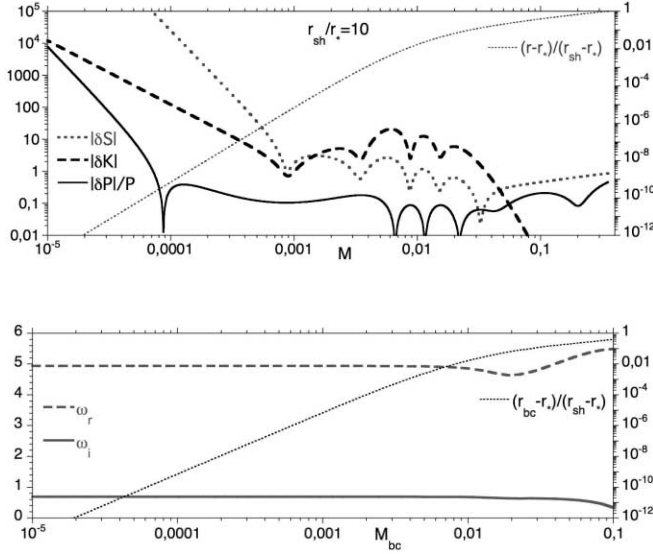


FIG. 2.—*Top*: Radial profiles of the perturbations of $|\delta K|$, $|\delta S|$, and $|\delta P|/P$ for the most unstable $l = 1$ mode, in the flow with $\alpha = 3/2$, $\beta = 5/2$, and $r_{sh}/r_* = 10$. The radial profiles are shown as a function of the Mach number M , with the corresponding value of the fractional radius shown on the right axis. *Bottom*: Influence of the radius r_{bc} , and associated Mach number M_{bc} , of the lower boundary on the complex eigenfrequency ω ; the very fine structure of the perturbations for $M < 4 \times 10^{-3}$ can be safely neglected.

(i.e., a fraction $< 0.1\%$ of the shock distance) have a negligible effect on the eigenfrequency.

If the advection time is infinite ($\alpha \geq \beta$), the boundary condition $\delta v/v = 0$ is applied at a radius where the advection time from the shock reaches 10 times the reference timescale $(r_{sh} - r_*)/|v_{sh}|$. We expect eigenmodes with a growth rate comparable to $|v_{sh}|/(r_{sh} - r_*)$ to be insensitive to any advective-acoustic artifact associated with this numerical prescription, because it occurs on a longer timescale than the instability. This expectation is validated by checking that the eigenfrequencies are unchanged by increasing the advection depth.

Once an eigenfrequency is found for a given intensity of the cooling function, it is tracked in the complex plane using the Newton-Raphson method. Eigenfrequencies are expressed in units of $|v_{sh}|/(r_{sh} - r_*)$ throughout the paper.

3.2. Comparison with the Eigenfrequencies Estimated by BM06

BM06 validated their numerical code in one dimension by comparing the eigenfrequency measured in the linear stage to the eigenfrequencies determined by HC92 for the mode $l = 0$ with $\alpha = 5/2$ and $\beta = 5/2$. Our calculation confirms this validation, as shown in Figure 3. Incidentally, Figure 3 shows that this flow is much more unstable to $l = 1$ perturbations than to radial ones. The nonspherical axisymmetric calculations of BM06 have been performed in a flow in which $\alpha = 3/2$ and $\beta = 5/2$, which was not considered by HC92. The eigenfrequencies of this flow are shown in Figure 4, with a globally acceptable agreement. The agreement seems significantly better for the $l = 0$ mode than non-radial ones. Figure 4 also shows that higher harmonics dominate the instability if the shock radius is large enough. For $r_{sh}/r_* = 5$ the instability of the mode $l = 1$ should be dominated by the first harmonics, whereas the mode $l = 2$ should be dominated by the second harmonics.

Figure 5 shows the expected growth rate in the flow with $\alpha = 6$ and $\beta = 1$ also considered by BM06, with a comparable agreement. Both Figures 4 and 5 enable us to evaluate the accuracy of numerical simulations; both the oscillation period

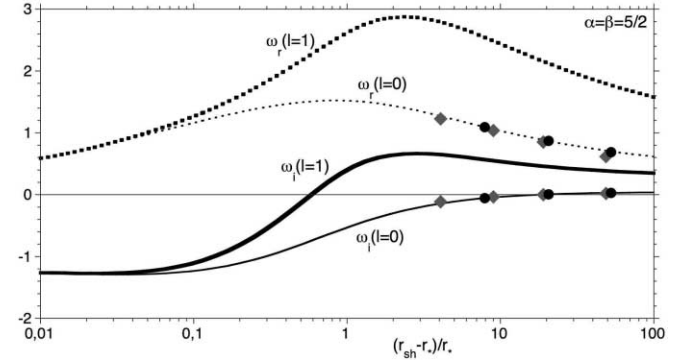


FIG. 3.—Oscillation frequency ω_r and growth rate ω_i of the fundamental modes $l = 0$ and 1 for $\alpha = \beta = 5/2$. Also shown are the $l = 0$ eigenfrequencies computed by HC92 (circles) and those measured in the one-dimensional simulation of BM06 (diamonds). The mode $l = 1$ is always more unstable than the radial mode in this flow.

and the growth time should be considered with a typical 30% uncertainty.

Some of the discrepancies can be attributed to difficulties in disentangling higher harmonics that have a similar growth rate. Whether part of this discrepancy could be attributed to numerical viscosity or not depends to some extent on our understanding of the instability mechanism. At low frequency, a purely acoustic mechanism should be barely sensitive to numerical viscosity. By contrast, a mechanism involving the advection of vorticity waves toward regions of small velocity may be more sensitive to numerical viscosity. This could contribute to explaining why the growth rate measured in the nonradial numerical simulations seems systematically lower than that predicted by the linear analysis. The radial profiles of δS and δK , displayed in Figure 2, show structures in the region of $M \sim 10^{-2}$, which cover $\sim 2\%$ of the

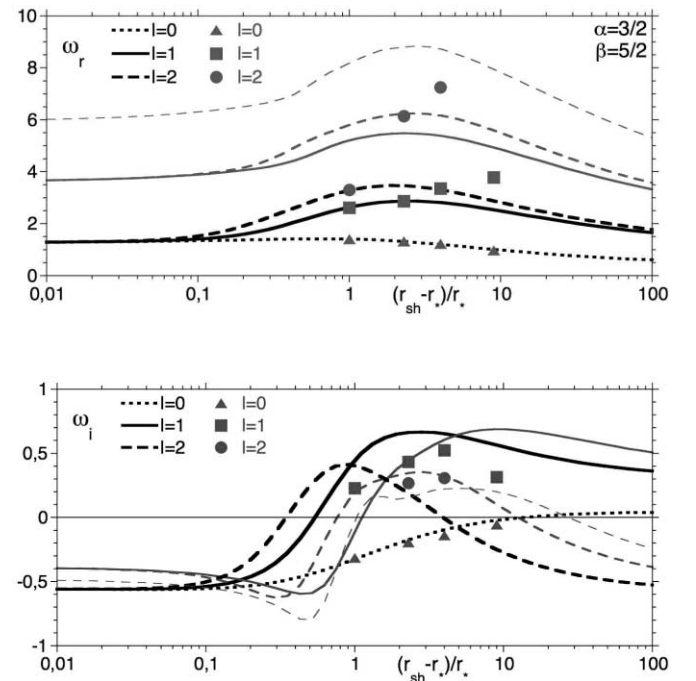


FIG. 4.—Eigenfrequencies for a cooling law with $\alpha = 3/2$ and $\beta = 5/2$, corresponding to the modes $l = 0$ (dotted line), $l = 1$ (solid line), and $l = 2$ (dashed line). The fundamental mode is plotted with thick black lines. Harmonics are shown with thinner gray lines. The eigenfrequencies determined from BM06 are shown as triangles ($l = 0$), squares ($l = 1$), and circles ($l = 2$).

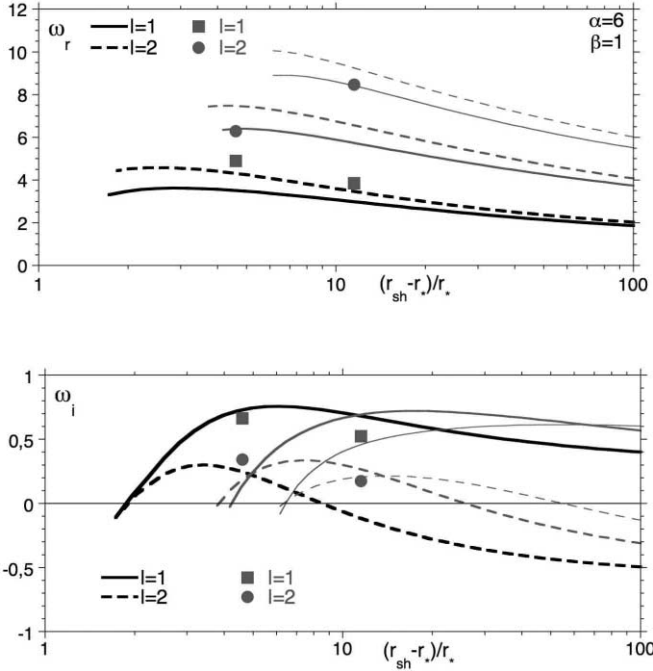


FIG. 5.—Same as Fig. 4, but for the cooling law $\alpha = 6$ and $\beta = 1$.

shock distance (see also Fig. 18, *bottom*). Given the difficulty of advecting vorticity waves in a grid-based code, a grid size of 0.1%–0.2% of the shock distance might be desirable near the accretor surface. Whether the 300–450 radial zones used in the simulations of BM06 are sufficient or not could be easily checked by performing new numerical simulations on a finer grid.

BM06 have pointed out the resemblance between the instability in these two flows despite the different cooling function. Although we agree on the resemblance between these two flows when the shock radius is large, Figure 5 reveals some significant differences for smaller shock radii:

1. The mode $l = 1$ is always the most unstable mode if $\alpha = 6$ and $\beta = 1$. By contrast, if $\alpha = 3/2$ and $\beta = 5/2$, the instability may be dominated by perturbations with a higher degree $l \geq 2$ if the shock radius is smaller than $2r_*$.

2. The flow with $\alpha = 6$ and $\beta = 1$ is stable if the shock radius is shorter than $\sim 2.5r_*$, whereas the flow with $\alpha = 3/2$ and $\beta = 5/2$ is unstable whatever the shock distance.

A more detailed investigation of the instability at small shock distance when $\alpha = 3/2$ and $\beta = 5/2$, illustrated by Figure 6, suggests that the most unstable mode corresponds to an azimuthal structure with a size comparable to the shock distance.

For both cooling functions, the dimensionless growth rate of the instability is at best on the order of 0.7–0.8:

$$\omega_i \leq \frac{|v_{\text{sh}}|}{r_{\text{sh}} - r_*}. \quad (25)$$

This similar growth rate can be viewed as a hint of a common physical mechanism of instability, which we investigate in § 4.

4. DETERMINATION OF THE INSTABILITY MECHANISM

4.1. Presence of Oscillations in the Eigenspectrum

The oscillation period and growth time associated with the most unstable eigenmode, as determined in Figures 4 and 5, should be

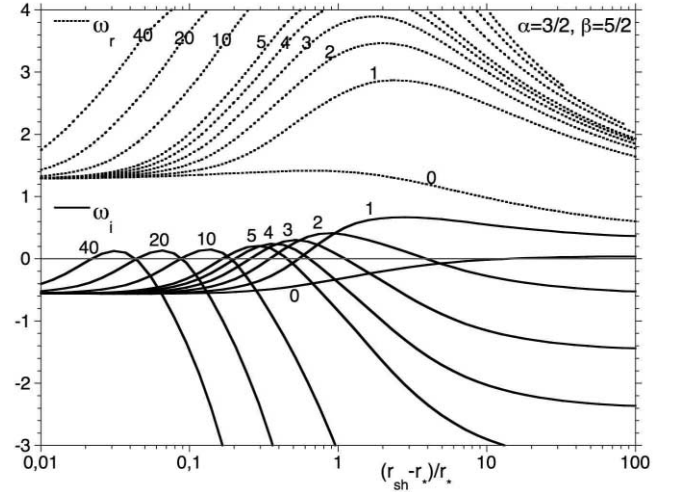


FIG. 6.—Eigenfrequencies corresponding to the fundamental modes $0 \leq l \leq 40$ for $\alpha = 3/2$ and $\beta = 5/2$. This plot indicates that the most unstable mode is always nonradial. The larger the shock radius, the smaller the degree $l \geq 1$ of the most unstable mode.

a signature of the instability mechanism. Unfortunately, our understanding of the possible instabilities is not deep enough to allow for a direct and conclusive interpretation of these time-scales. The linear stability analysis can be helpful in determining the underlying mechanism, using the many other eigenfrequencies of the eigenspectrum. A global view of the eigenspectrum associated with $l = 1$ perturbations is shown in Figure 7 for both cooling functions, with different shock distances. Figure 7 suggests that the larger the shock radius, the more numerous the unstable modes. A striking feature of these eigenspectra is the oscillation of the growth rate, which is easier to identify when the number of well-defined eigenmodes is large, i.e., when the shock radius is large. According to Figure 7, this identification requires $r_{\text{sh}}/r_{\nabla} > 10$ if $\alpha = 6$ and $\beta = 1$, whereas the oscillations are already

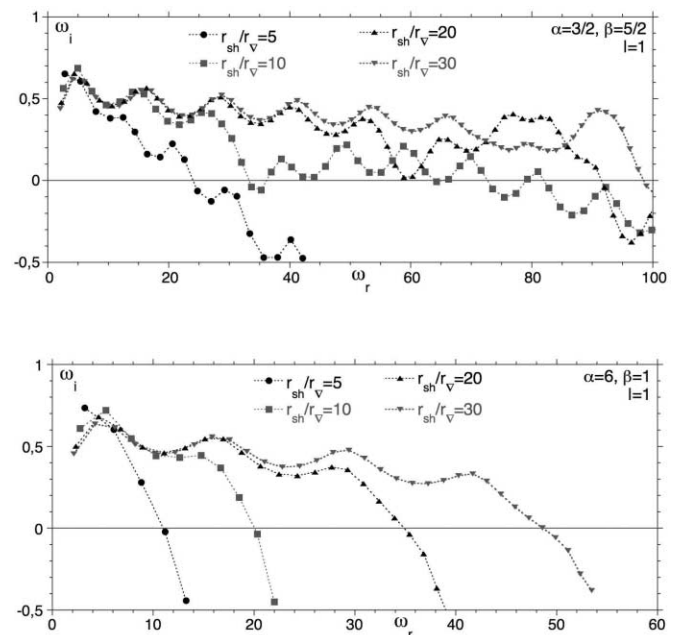


FIG. 7.—Eigenfrequencies computed from the boundary value problem in a flow with $\alpha = 3/2$ and $\beta = 5/2$ (*top*) and $\alpha = 6$ and $\beta = 1$ (*bottom*) for different shock radii r_{sh}/r_{∇} for $l = 1$ perturbations.

visible for $r_{\text{sh}}/r_* = 5$ if $\alpha = 3/2$ and $\beta = 5/2$. These eigenspectrum oscillations are reminiscent of the oscillations visible in the eigenspectrum of the isothermal accretion flow accelerated toward a black hole (Fig. 4 of F02). They were explained by F02 as a consequence of the influence of a purely acoustic cycle interacting either constructively or destructively with the advective-acoustic cycle. The efficiencies of these two cycles are measured in § 4.2, after recalling the formalism associated with these cycles.

4.2. Calculation of the Efficiencies \mathcal{Q} and \mathcal{R} of the Advective-Acoustic and Purely Acoustic Cycles

4.2.1. Advective-Acoustic and Purely Acoustic Cycles

F02 developed a formalism in order to describe the advective-acoustic cycle, stable or not, below a stationary shock in a radial accretion flow onto a black hole. The same formalism can be applied to a decelerated accretion flow onto a hard surface. Let us recall that vorticity and entropy perturbations are advected at the velocity of the flow, whereas pressure perturbations can propagate at the speed of sound. These two categories of perturbations would be linearly independent in a uniform flow but are coupled linearly if the flow is inhomogeneous. The interaction between the stationary shock and the flow gradients gives birth to two cycles:

1. An advective-acoustic cycle, whose duration is denoted by τ_Q . An advected perturbation of frequency ω_r generates a pressure feedback, which triggers, at the shock, a new advected perturbation, whose amplitude has changed by a factor $\mathcal{Q}(\omega_r)$ after one advective-acoustic cycle.

2. A purely acoustic cycle, whose duration is denoted by τ_R . An acoustic perturbation of frequency ω_r propagating downward (not necessarily radially) produces a reflected (or refracted) perturbation reaching the shock and triggers a new pressure perturbation, whose amplitude has changed by a factor $\mathcal{R}(\omega_r)$ after one acoustic cycle.

The “vortical-acoustic” instability studied by F02 is fundamentally nonradial, because vorticity perturbations are the only advected perturbations in an isothermal flow. In a gas with $\gamma = 4/3$, the advective-acoustic cycles exist for both radial and non-radial perturbations. A radial advective-acoustic cycle relies entirely on entropy perturbations. In an adiabatic flow, the acoustic feedback depends on the global increase of enthalpy in the post-shock flow (Foglizzo & Tagger 2000; F01) and can be efficient enough to destabilize the Bondi-Hoyle-Lyttleton accretion (Foglizzo et al. 2005). The instability of this “entropic-acoustic” cycle (i.e., the mode $l = 0$) is disfavored in the core-collapse context because neutrino cooling precludes a strong adiabatic heating.

4.2.2. Eigenfrequencies Associated with the Cycles

The simplest formulation of the advective-acoustic instability corresponds to a situation in which the purely acoustic cycle is negligible. The instability threshold then corresponds to $|\mathcal{Q}| = 1$, and the growth rate ω_i can be approximated by

$$\omega_i \sim \frac{1}{\tau_Q} \log |\mathcal{Q}|. \quad (26)$$

More generally, Foglizzo & Tagger (2000) showed that the purely acoustic cycle is not necessarily negligible and modifies equation (26) as follows:

$$\mathcal{Q}e^{i\omega\tau_Q} + \mathcal{R}e^{i\omega\tau_R} = 1. \quad (27)$$

This equation describing the simultaneous existence of two cycles (\mathcal{Q}, τ_Q) and (\mathcal{R}, τ_R) is symmetric; it can account for an advective-acoustic instability ($|\mathcal{Q}| > 1$), as well as a hypothetical acoustic instability (if $|\mathcal{R}| > 1$). In the isothermal flow studied by F02, the acoustic cycle is “weak” in the sense that the parameter $\epsilon < 1$:

$$\epsilon \equiv \frac{|\mathcal{R}|}{|\mathcal{Q}|^{\tau_R/\tau_Q}} < 1. \quad (28)$$

Assuming $\epsilon < 1$, F02 showed from equation (27) that the effect of the acoustic cycle is to either increase or decrease the growth rate ω_i in the following range:

$$\frac{1}{\tau_Q} \log \frac{|\mathcal{Q}|}{1 + \epsilon} < \omega_i < \frac{1}{\tau_Q} \log \frac{|\mathcal{Q}|}{1 - \epsilon}. \quad (29)$$

The case $\epsilon > 1$ would be exactly symmetric by exchanging (\mathcal{Q}, τ_Q) and (\mathcal{R}, τ_R) in equations (28) and (29).

4.2.3. How to Extract the Cycles Information Directly from the Eigenspectrum

Assuming that the underlying mechanism is due to a superposition of cycles described by equation (27), an estimate of \mathcal{Q} , \mathcal{R} , τ_Q , and τ_R can be extracted directly from the oscillations observed in the eigenspectrum in Figure 7. This method enables us to identify two cycles, one slow and one fast, and measure their efficiencies. For the sake of simplicity we choose to denote the fast cycle with the letter \mathcal{R} and the slow one with the letter \mathcal{Q} (i.e., $\tau_Q > \tau_R$). The identification of the slow cycle with the advective-acoustic mechanism and the fast cycle with the purely acoustic mechanism becomes unambiguous in § 4.2.4, which also validates the assumption of an equation (27) underlying the eigenspectrum.

According to F02, the timescale τ_Q of the slowest cycle is related to the frequency difference $\omega_r(i+1) - \omega_r(i)$ between two consecutive eigenmodes, whereas the shortest timescale τ_R is related to the frequency range $\Delta\omega_r$ of each oscillation. Denoting by n_{osc} the number of eigenmodes per oscillation,

$$\tau_Q \sim \frac{2\pi}{\omega_r^{i+1} - \omega_r^i}, \quad (30)$$

$$\frac{\tau_Q}{\tau_R} \sim n_{\text{osc}}. \quad (31)$$

For example, at first glance on Figure 7 (top), one can anticipate that $\tau_Q/\tau_R \sim 5$ if $r_{\text{sh}}/r_* = 5$, whereas $\tau_Q/\tau_R \sim 10$ if $r_{\text{sh}}/r_* = 30$.

According to equations (54) and (55) of F02, the efficiencies $|\mathcal{Q}|$ and $|\mathcal{R}|$, associated with the slow and fast cycles, respectively, can be extracted directly from the eigenspectrum by measuring the following parameters of the eigenspectrum oscillations: (1) the frequency range $\Delta\omega_r$ of each oscillation, (2) the number n_{osc} of eigenmodes per oscillation, (3) the amplitude $\Delta\omega_i$ of the oscillations of the growth rate, and (4) their average value $\bar{\omega}_i$:

$$|\mathcal{Q}| = \frac{\cosh \pi \Delta\omega_i / \Delta\omega_r}{\cosh (n_{\text{osc}} - 1) \pi \Delta\omega_i / \Delta\omega_r} \exp 2n_{\text{osc}} \pi \frac{\bar{\omega}_i}{\Delta\omega_r}, \quad (32)$$

$$|\mathcal{R}| = \frac{\sinh n_{\text{osc}} \pi \Delta\omega_i / \Delta\omega_r}{\cosh (n_{\text{osc}} - 1) \pi \Delta\omega_i / \Delta\omega_r} \exp 2\pi \frac{\bar{\omega}_i}{\Delta\omega_r}. \quad (33)$$

The result of this method, applied to the $l = 1$ eigenmodes of Figure 7, is shown in Figure 8 for $\alpha < \beta$ and in Figure 9 for $\alpha > \beta$. It shows that the fast cycle (diamonds) is always stable,

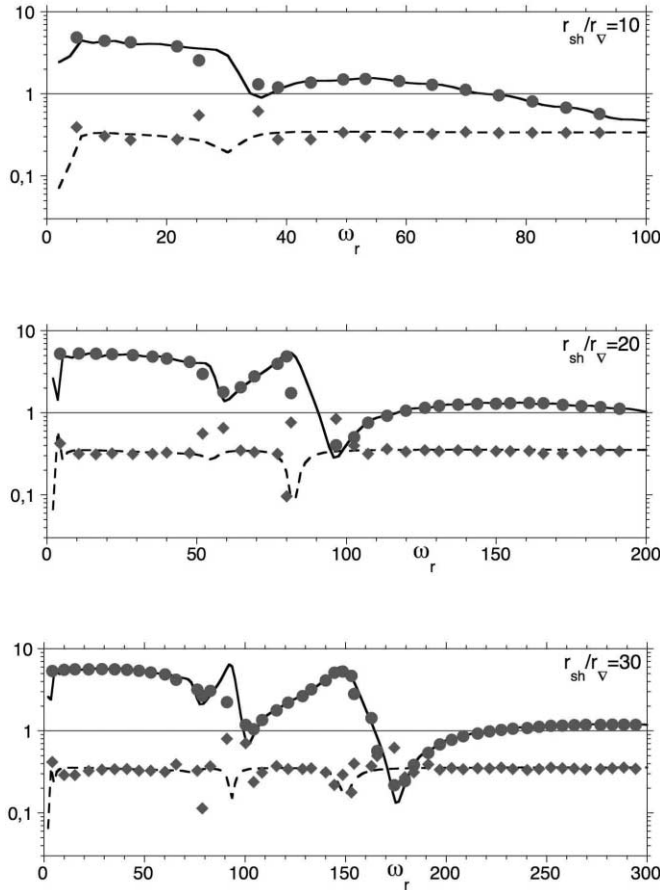


FIG. 8.— Comparison between the coupling efficiencies $|Q|(\omega)$ and $|R|(\omega)$ of the mode $l = 1$, computed in the WKB approximation (solid and dashed lines) and the ones deduced from the eigenspectrum (circles and diamonds) using eqs. (32) and (33) in a flow with $\alpha = 3/2$ and $\beta = 5/2$ for different shock radii r_{sh}/r_* . The agreement validates the formalism associated with the two cycles. The acoustic cycle is stable ($|R| < 1$), and the advective-acoustic cycle can be unstable ($|Q| \sim 4-6$).

whereas the slow cycle (circles) can be unstable. We now proceed to check the validity of these results by computing $|Q|$ and $|R|$ using another method, which will establish that the fast stable cycle is purely acoustic, and the slow cycle is advective-acoustic.

4.2.4. An Alternate Way to Measure $|Q|$ and $|R|$, in the WKB Approximation

Following F02, this method consists of determining the coupling efficiencies $|Q|$ and $|R|$ as continuous functions of the perturbation frequency ω_r . The efficiency of the acoustic cycle is decomposed into $R \equiv R_{sh}R_{\nabla}$, while the efficiency of the advective-acoustic cycle is decomposed into $Q \equiv Q_{sh}Q_{\nabla}$, with R_{sh} , R_{∇} , Q_{sh} , and Q_{∇} being defined as follows:

1. When an acoustic wave of frequency ω_r propagating outward reaches the shock, $R_{sh}(\omega_r)$ measures the efficiency of acoustic reflection, while $Q_{sh}(\omega_r)$ measures the amount of advected perturbations (entropy/vorticity) produced by the shock.

2. When an acoustic wave of frequency ω_r propagates in the flow toward the accretor, $R_{\nabla}(\omega_r)$ measures the amount of acoustic reflection. When an advected perturbation of frequency ω_r is advected toward the accretor, $Q_{\nabla}(\omega_r)$ measures the amount of acoustic waves propagating against the flow. Note that Q_{∇} and R_{∇} are measured at a radius immediately below the shock but do not involve the physics of the shock.

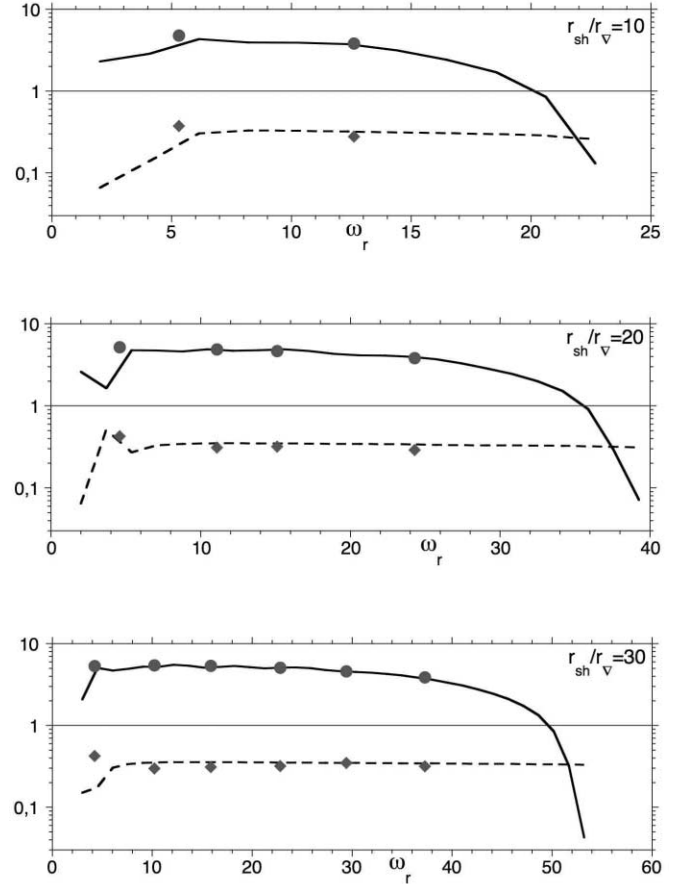


FIG. 9.— Same as Fig. 8, but with a different cooling function: $\alpha = 6$ and $\beta = 1$. The efficiencies $|Q|$ and $|R|$ are similar to those obtained with $\alpha = 3/2$ and $\beta = 5/2$.

This approach is an extension of the approach used by F01 and F02 in adiabatic and isothermal flows, where acoustic and advected perturbations are easily identified using a WKB approximation. The technicalities of the method are described in Appendices C and D. The WKB approach assumes that the wavelength of the advected and acoustic perturbation is shorter than the scale of the flow gradients just below the shock. This method is thus expected to be reliable at high frequency and to break down at low frequency.

Besides, the presence of cooling processes makes this method even more approximative, since we choose to neglect it in the immediate vicinity of the shock for the sake of simplicity. Neglecting cooling is certainly justified when the shock is far enough from the accretor, as illustrated by the flat entropy profile in Figure 1 (top) for $r_{sh}/r_{\nabla} = 5$.

The results of the WKB analysis applied to the $l = 1$ mode are displayed as solid and dashed lines in Figures 8 and 9, together with the results of the first method. The agreement between the two methods is excellent at frequencies where $|Q|$ and $|R|$ vary smoothly with frequency. Since the method based on the eigenspectrum requires several neighboring eigenmodes to determine $|Q|$ and $|R|$, it is unable to correctly capture variations that are faster than the oscillation period $\Delta\omega_r$. This is particularly visible in the resulting estimate of $|R|$ in Figure 8.

The direct method used in § 4.2.3 can be used to estimate the range of validity of the WKB approximation. A close inspection of Figures 8 and 9 suggests that the WKB approximation is acceptable for $\omega_r \geq 5$ in both flows.

Both methods indicate that the purely acoustic is stable and is not even close to the instability threshold, with typical values

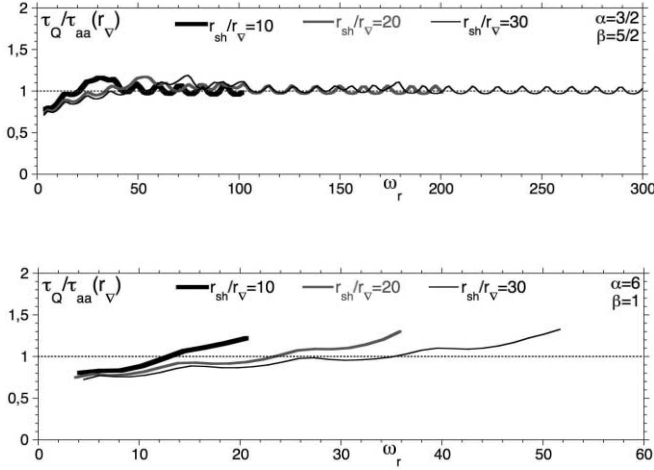


FIG. 10.—Estimate of the cycle timescale τ_Q , directly extracted from the eigenspectrum (eq. [30]). It is measured in units of the radial advective-acoustic time $\tau_\nabla \equiv \tau_{aa}(r_\nabla)$ down to the radius r_∇ of maximum velocity gradient. At low frequency, the cycle timescale is 20% shorter than $\tau_{aa}(r_\nabla)$.

$|\mathcal{R}| \leq 0.5$. If a purely acoustic mechanism were responsible for the low-frequency instability, as proposed by BM06, this mechanism would have to be stable at higher frequency to be compatible with the results of our analysis.

More importantly, our calculations prove that the advective-acoustic cycle is unstable in the range of frequencies accessible to our analysis, with an efficiency reaching $|\mathcal{Q}| \sim 4-6$. The next sections aim at characterizing the properties of this instability by estimating the timescale τ_Q of the cycle and the effective coupling radius r_{eff} (§ 4.3) and finding approximations for its growth rate (§ 4.4) and oscillation period (§ 4.5). Whether this instability mechanism is responsible for the dominant low-frequency mode is discussed in § 5.

4.3. Estimate of the Timescale τ_Q and Effective Coupling Radius r_{eff} of the Advective-Acoustic Cycle

The accurate determination of the cycle timescales τ_Q and τ_R , using the velocity and sound speed profiles of the stationary flow, is not straightforward; the duration τ_R of the acoustic cycle depends on the depth of the turning point and is thus a function of both the frequency ω_r and the order l . Similarly, ω_r and l influence the depth at which an advected perturbation couples most efficiently to acoustic perturbations. The study of the advective-acoustic coupling in an adiabatic or isothermal flow showed that this coupling occurs all the way from the shock to the accretor (eq. [25] of F01; eq. [29] of F02). Its net effect viewed from the shock radius can be summarized as a feedback from a single effective radius of coupling r_{eff} , associated with an advective-acoustic timescale τ_Q . Let us define two radial reference timescales in the stationary flow:

1. The radial acoustic timescale $\tau_{\text{ac}}(r)$ from the shock to the radius r and return:

$$\tau_{\text{ac}}(r) \equiv \int_{\text{sh}}^r \frac{2}{1 - \mathcal{M}^2} \frac{dr}{c}. \quad (34)$$

2. The radial advective-acoustic timescale $\tau_{\text{aa}}(r)$, defined as the advection timescale from the shock to the radius r , and acoustic return in the radial approximation:

$$\tau_{\text{aa}}(r) \equiv \int_{\text{sh}}^r \frac{1}{1 - \mathcal{M}} \frac{dr}{\mathcal{M}c}. \quad (35)$$

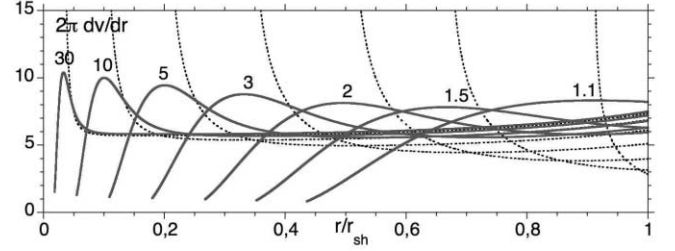


FIG. 11.—Radial profile of the velocity gradient $2\pi dv/dr$, for different stationary flows, for both sets of cooling parameters $\alpha = 3/2$ and $\beta = 5/2$ (dotted lines) and $\alpha = 6$ and $\beta = 1$ (solid lines). Each line is labeled by the ratio r_{sh}/r_∇ . The velocity gradient is normalized by $|v_{\text{sh}}|/(r_{\text{sh}} - r_*)$.

The nonradial character of the acoustic feedback has a minor influence on $\tau_{\text{aa}}(r)$, given the subsonic character of the flow. By contrast, BM06 noted that the acoustic time for a very nonradial, purely acoustic wave can be significantly longer than along a radial path; the shock circumference is indeed a factor of π longer than its diameter.

In Figure 10 we find it convenient to measure the cycle timescale τ_Q deduced from equation (30), in units of $\tau_\nabla \equiv \tau_{aa}(r_\nabla)$, where r_∇ is the radius defined in § 2.1 and the velocity gradient is maximum. The globally good matching between these two timescales indicates that velocity gradients are an important ingredient for the advective-acoustic coupling responsible for the acoustic feedback, as in the vortical-acoustic instability studied in an isothermal context by F02. Note that temperature gradients may also contribute to the advective-acoustic coupling, as seen in the adiabatic study of F01.

We should keep in mind, however, that r_∇ is defined as a local maximum, whereas our definition of r_{eff} is global in the sense that it involves both the local coupling efficiency and the advection/propagation of the perturbations between the shock and r_{eff} . In consequence, the approximation $r_{\text{eff}} \sim r_\nabla$ should be viewed as a guide to our intuition rather than a fundamental property.

An advected perturbation of oscillation frequency ω_r is most sensitive to flow gradients whose length scale is shorter than the wavelength $2\pi v/\omega_r$. The length scale associated with velocity gradients scale like $(dv/vdr)^{-1}$:

$$\omega_r < 2\pi \frac{dv}{dr}. \quad (36)$$

According to Figure 11, the velocity gradient in the flow with $\alpha > \beta$ is very smooth and spread when the shock distance is short, whereas it gets sharper when the shock distance is large. This may explain, at least qualitatively, why the flow with $\alpha = 6$ and $\beta = 2$ is stable for $r_{\text{sh}}/r_* < 2.6$, whereas the flow with $\alpha = 3/2$ and $\beta = 5/2$ is unstable even for a small shock distance.

Similarly, the divergence of the velocity gradient in the flow $\alpha < \beta$ is likely to couple advected and acoustic perturbations at much higher frequencies than in the flow $\alpha > \beta$, where the velocity gradient is smoother. This qualitative argument may explain why the range of unstable frequencies is so much larger for $\alpha = 3/2$ and $\beta = 5/2$ than for $\alpha = 6$ and $\beta = 1$ (as visible in Fig. 7 and summarized in Fig. 16).

Figure 11 also illustrates the fact that velocity gradients are present all the way from the shock to r_∇ and may affect perturbations with a low frequency $\omega_r < 5$, according to equation (36). This threshold is comparable to our estimate of the threshold of the WKB approximation in § 4.2.4.

We interpret the 20% offset visible in Figure 10 at low frequency as a consequence of the coupling through the various

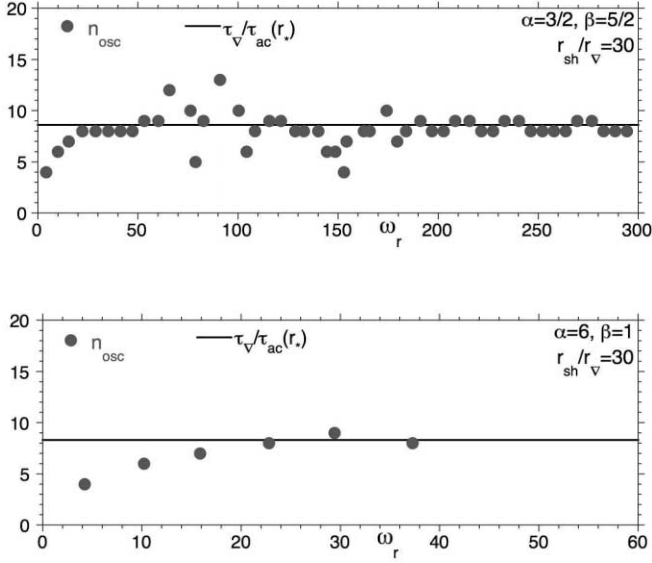


FIG. 12.—Comparison between the number n_{osc} of eigenmodes per eigenspectrum oscillation and the ratio of timescales $\tau_Q/\tau_{\text{ac}}(r_*)$ for the two cooling functions with $r_{\text{sh}}/r_{\text{v}} = 30$.

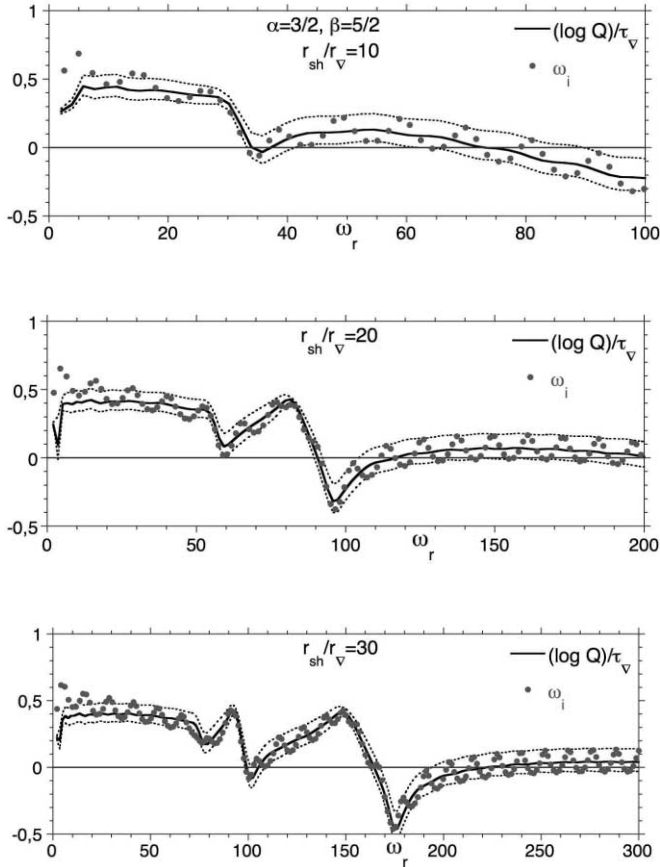


FIG. 13.—Comparison between the eigenfrequencies computed from the boundary value problem and the first-order estimate $(\log Q)/\tau_{\text{v}}$ in a flow with $\alpha = 3/2$ and $\beta = 5/2$ for different shock distances $r_{\text{sh}}/r_{\text{v}}$. The dotted lines correspond to the minimum and maximum growth rates described by eq. (29), in which τ_Q/τ_{R} is approximated by $\tau_{\text{v}}/\tau_{\text{ac}}(r_*)$.

flow gradients, including velocity, above r_{v} . Keeping in mind this low-frequency distortion, the timescale τ_{v} can be considered an acceptable approximation of τ_Q for unstable $l = 1$ modes.

4.4. First-Order Approximation of the Growth Rate

Finding a discrete set of eigenmodes is a laborious task, in comparison with the straightforward calculation of $|\mathcal{Q}|$ and $|\mathcal{R}|$ in the WKB approximation. In this respect, equation (29) provides us with a useful estimate of the growth rate if the parameters of the cycle τ_Q , τ_{R} , $|\mathcal{Q}|$, and $|\mathcal{R}|$ are known. Although our estimate τ_{v} of τ_Q is not fully satisfactory, we can continue along this direction in order to check what kind of accuracy can be reached. The effect of the acoustic cycle described by equation (29) depends through ϵ on the ratio τ_Q/τ_{R} (eq. [28]), which is measured by n_{osc} (eq. [31]). Despite the potentially significant difference between the timescales of radial and nonradial acoustic modes, we choose to approximate τ_{R} by $\tau_{\text{ac}}(r_*)$ and compare in Figure 12 the number n_{osc} measured on the eigenspectra of Figure 7 to the reference ratio $\tau_{\text{v}}/\tau_{\text{ac}}(r_*)$. The global agreement is acceptable given the discreteness of the number of nodes, the gross approximation of τ_{R} by $\tau_{\text{ac}}(r_*)$, and the difficulty of identifying the oscillation, especially when Q varies rapidly near $\omega_r \sim 90$ and ~ 150 for $\alpha = 3/2$ and $\beta = 5/2$. The systematic decrease of n_{osc} observed at low frequency is compatible with the decrease of τ_Q/τ_{v} discussed in § 4.3.

The growth rate ω_i measured in the eigenspectra of Figure 7 is then compared in Figures 13 and 14 to the value $(\log Q)/\tau_{\text{v}}$ (solid line) and the expected range of influence of the acoustic

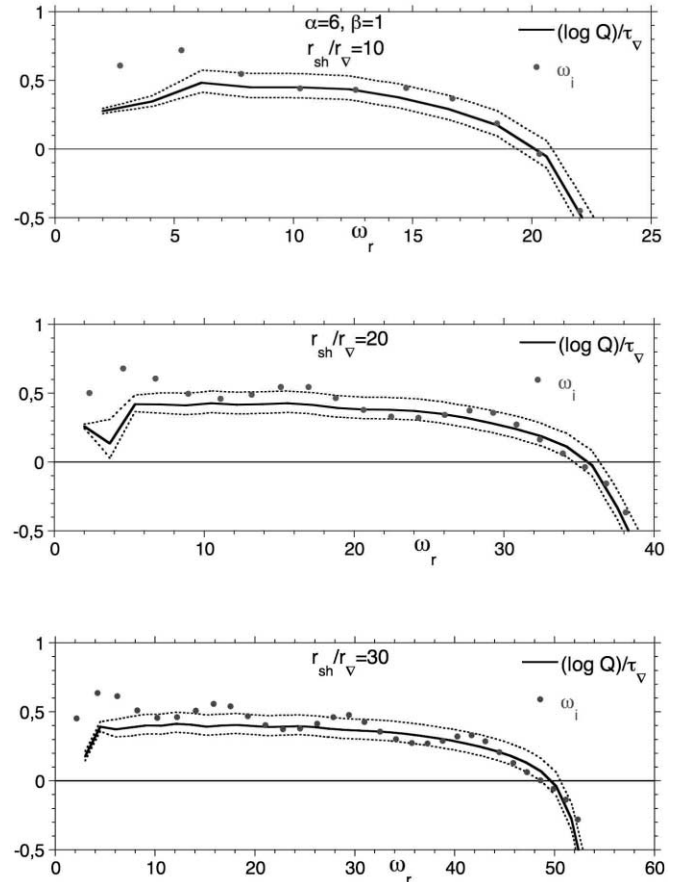


FIG. 14.—Same as Fig. 13, but with a different cooling function: $\alpha = 6$ and $\beta = 1$.

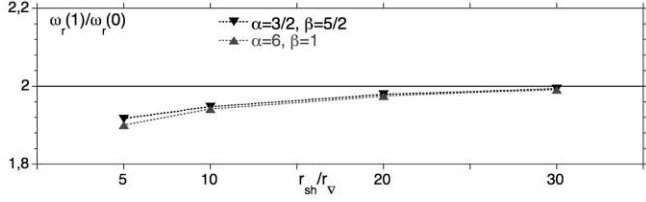


FIG. 15.—Ratio of the frequencies of the first two eigenmodes $\omega_r(1)/\omega_r(0)$ corresponding to $l = 1$ perturbations; the oscillation period $2\pi/\omega_r$ of the fundamental mode is an excellent measure of the advective-acoustic timescale τ_Q .

cycle deduced from equation (29) (dotted lines). This comparison is interpreted as follows:

1. The amplitude of the eigenspectrum oscillation is very well matched by equation (29).
2. The global shape of the eigenspectrum is globally very well reproduced.
3. As expected, some systematic discrepancies are observed at low frequency concerning the first ~ 10 eigenmodes. This discrepancy can reach a factor of 2 for the fundamental mode.

We first conclude that the radius r_∇ is an excellent approximation of the feedback radius at high frequency for both cooling functions. This provides us with a rather simple description of the instability mechanism at work at high frequency.

The discrepancy observed at very low frequency exceeds the 20% effect due to overestimating τ_Q , because the WKB approximation used to compute $|Q|$ and $|R|$ ceases to be valid, as already pointed out in § 4.2.4. Figures 13 and 14 suggest that the WKB approximation can only provide a gross estimate of the growth rate of the lowest frequency modes, within a factor of 2.

4.5. Oscillation Timescale and Efficiency $|Q|$ Associated with the Most Unstable Mode

The relationship between the oscillation period of the fundamental mode and the timescale of the cycle is not obvious a priori, even if the acoustic cycle is neglected, because it depends on the phase ϕ_Q of the complex efficiency Q . Denoting by $\omega_r(k)$ the frequency of the k th harmonic, the phase relation associated with equation (27) when the acoustic cycle is neglected leads to

$$\omega_r(k)\tau_Q + \phi_Q = 2(k+1)\pi. \quad (37)$$

A comparison of the frequency $\omega_r(k=0)$ of the fundamental mode with the frequency of the first harmonic $\omega_r(k=1)$, shown in Figure 15, indicates that $\omega_r(1) \sim 2\omega_r(0)$. We conclude that the phase of Q is negligible and that the oscillation period of the fundamental mode is a good measure of the timescale τ_Q at low frequency.

The fundamental mode is not always the most unstable one among the $l = 1$ perturbations; Figure 16 summarizes the frequency range of unstable modes for $\alpha = 3/2$ and $\beta = 5/2$ (top) and $\alpha = 6$ and $\beta = 1$ (bottom). The most unstable mode may correspond to either the fundamental mode, the first harmonic, or the second harmonic as the shock radius increases from $r_{sh}/r_\nabla = 1.5$ to 100. For both sets of cooling parameters, the corresponding oscillation period $2\pi/\omega_r$ of the most unstable $l = 1$ mode would therefore be τ_Q for $1.5 < r_{sh}/r_\nabla < 5-6$, $\tau_Q/2$ for $5-7 < r_{sh}/r_\nabla < 33-39$, and even $\tau_Q/3$ for $r_{sh}/r_\nabla > 33-39$.

An upper bound of the efficiency $|Q|$ associated with the low-frequency modes can be estimated from equation (26) by ne-

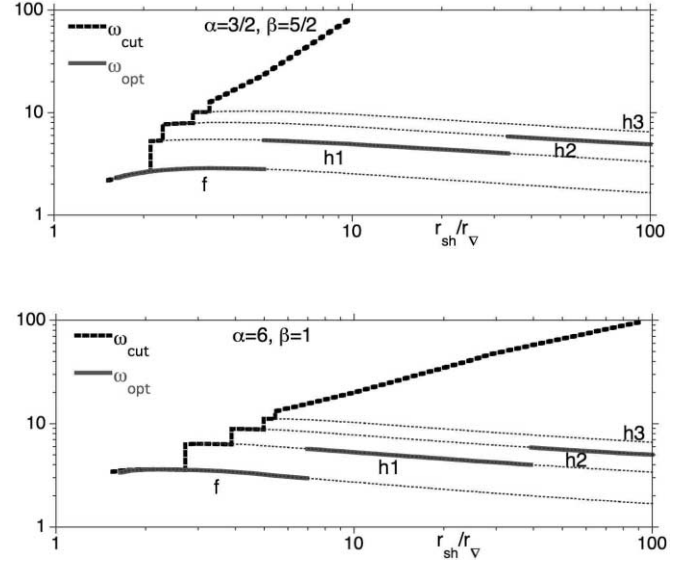


FIG. 16.—Range of unstable frequencies of the $l = 1$ mode. The frequency of the most unstable mode (solid line) corresponds to one of the first harmonics denoted by “f,” “h1,” and “h2.” The cutoff frequency (dashed thick line) is a steeper function of the shock radius in the flow with $\alpha < \beta$.

glecting the purely acoustic cycle and approximating $\tau_Q \sim 2\pi(k+1)/\omega_r(k)$. The value of $\exp(\omega_r\tau_Q)$ is shown in Figure 17 for the first three eigenfrequencies “f,” “h1,” and “h2” as a function of the shock radius. The actual value of Q at large shock radius is likely to be intermediate between line f and line h1 in Figure 17 for $10 \leq r_{sh}/r_\nabla \leq 30$, as suggested by Figure 7; indeed, the eigenspectrum oscillation at low frequency in Figure 7 suggests that the first harmonics h1 and h2 benefit from a constructive influence of the acoustic cycle, whereas this influence seems destructive on the fundamental mode f. In this respect, Figure 17 indicates that $|Q|_{\text{WKB}}$ can be used as an acceptable guess of the efficiency $|Q|$ at low frequency.

Besides, Figure 17 suggests a slow increase of the efficiency $|Q|$ with the shock radius, with remarkable similarity for the two sets of cooling parameters (solid and dashed lines). As the shock radius is increased, the slow increase of the oscillation frequency of the most unstable mode (Fig. 16) and the increase of $|Q|$ (Fig. 17) are not explained yet.

5. CONTINUITY ARGUMENT FOR THE ADVECTIVE-ACOUSTIC INSTABILITY AT LOW FREQUENCY

Strictly speaking, we have demonstrated that the advective-acoustic cycle is responsible for the high-frequency $l = 1$ instability of a stalled accretion when it is far enough from the accretor for two different types of cooling functions. What is the bearing

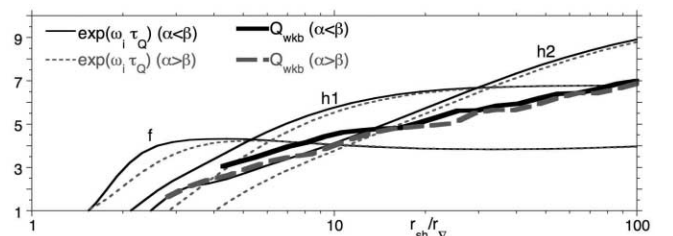


FIG. 17.—Maximum efficiency $|Q|_{\text{WKB}}$ of $l = 1$ perturbations in the WKB approximation (thick lines) compared to $\exp(\omega_r\tau_Q)$ of the low-frequency eigenmodes f, h1, and h2. The cycle timescale is approximated as $\tau_Q \sim 2\pi(k+1)/\omega_r(k)$.

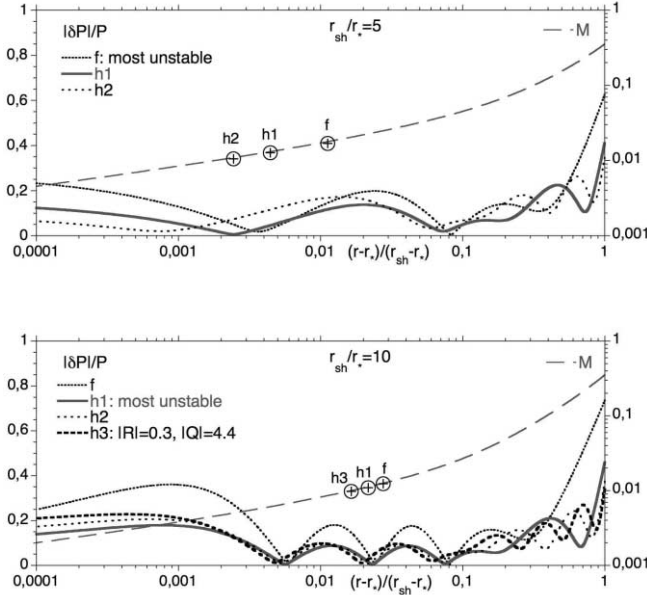


FIG. 18.—Radial profiles of the pressure perturbation $|\delta P|/P$ for the fundamental $l = 1$ mode (f) and its first harmonics ($h1, h2, \dots$) in the flow with $\alpha = 3/2$, $\beta = 5/2$, and $r_{sh}/r_* = 5$ (top) and $r_{sh}/r_* = 10$ (bottom). The pressure profile is shown as a function of the fractional radius, with the corresponding Mach number shown on the right axis. In the flow with $r_{sh}/r_* = 10$, the frequency of the third harmonic $h3$ is high enough to establish the instability of the advective-acoustic cycle $|\mathcal{Q}| = 4.4$ and the stability of the purely acoustic cycle $|\mathcal{R}| = 0.3$ (Fig. 8, top). The shapes of all these functions look very similar, suggesting a common physical mechanism. A lower bound of the position of the effective coupling radius r_{eff} is indicated by a circled plus symbol, corresponding to $\tau_{adv}(r) = 2\pi(k+1)/\omega_r$ for the k th harmonic.

of this demonstration on the instability mechanism of the low-frequency modes when the shock radius is moderate? Since the analysis of the fundamental $l = 1$ mode and its first harmonics is intractable through the usual WKB techniques, one might argue that the instability mechanism of the fundamental mode is out of reach of the present study. The eigenspectrum of the flow with $\alpha = 6$, $\beta = 1$, and $r_{sh}/r_{\nabla} = 5$ (Fig. 7, bottom) contains too few unstable modes to allow for the identification of oscillations, and the frequency of these eigenmodes is too low to allow for a WKB analysis. In this case, neither of the two methods described in § 4.2 is able to compute $|\mathcal{Q}|$ and $|\mathcal{R}|$. Figure 7, however, shows the continuity of the shape of the eigenspectrum, both with respect to frequency and with respect to the shock radius. The growth rate of the low-frequency eigenmodes is only marginally larger than those at higher frequency. We feel there is no need to invoke a different instability mechanism at low frequency given the smooth distribution of growth rates. According to Figure 7, decreasing the shock radius seems to reduce the cutoff frequency above which the modes are stable but barely affects the growth rate of the low-frequency modes. The continuity of the flow properties with respect to the shock radius is also apparent in the sequence of plots in Figures 8–9 and 13–14.

Besides, the radial structure of the pressure perturbation looks very similar for all the harmonics displayed in Figure 18 for two different shock radii. The eigenfunction of the low-frequency, most unstable mode resembles those of higher frequency modes for which a reliable determination of the cycle efficiencies \mathcal{Q} and \mathcal{R} is possible. The similarity of the eigenfunctions suggests again a common instability mechanism for all these modes, namely, the instability of the advective-acoustic cycle.

Could the same kind of mechanism account for the slow instability of the fundamental $l = 0$ mode, observed in Figures 4 or

6 for a large shock radius $r_{sh}/r_* > 15$? The eigenspectrum associated with the radial mode shows oscillations very similar to Figure 7, except that all the higher harmonics are stable, even for a very large shock radius $r_{sh}/r_* = 1000$. These oscillations enable the direct computation of the efficiencies $|\mathcal{Q}|$ and $|\mathcal{R}|$ of the acoustic cycle. The entropic-acoustic cycle is always stable, $|\mathcal{Q}| < 1$, at the high frequencies required by the WKB analysis, and the purely acoustic cycle is also stable, $|\mathcal{R}| < 1$. Since the first harmonics seem always stable, the instability mechanism of the fundamental $l = 0$ mode is more difficult to interpret than for $l = 1$ modes. We cannot exclude, however, that it may be due to a low-frequency entropic-acoustic cycle destabilized by the temperature increase in the adiabatic part of the flow, when the shock radius is large.

6. DISCUSSION OF THE ACOUSTIC INTERPRETATION OF BM06

BM06 summarized their preference for a purely acoustic mechanism with the following three observations:

1. The advection time down to the accretor surface $\tau_{adv}(r_*)$ is larger than the oscillation period $\tau_{osc} \equiv 2\pi/\omega_r$, whereas a nonradial path exists such that the acoustic timescale along this path coincides with τ_{osc} (Fig. 6 of BM06).
2. A standing $l = 1$ acoustic wave is clearly visible on the pressure profile. The particular radius r such that $\tau_{adv}(r) \sim \tau_{osc}$, which could have been identified as a radius of effective advective-acoustic coupling, does not show any particular signature on the pressure profile.
3. The instability seems independent of the flow near the accretor, given the resemblance between the results with the two different cooling functions, which differ only in the innermost regions.

We believe that part of the confusion comes from the fact that for a postshock Mach number $\mathcal{M}_{sh} \sim 1/8^{1/2}$ typical of a strong adiabatic shock with $\gamma = 4/3$, the advection timescale r_{sh}/v_{sh} happens to be both longer than the radial acoustic timescale $2r_{sh}/c_{sh}$ and shorter than the surface acoustic time $2\pi r_{sh}/c_{sh}$:

$$\frac{2r_{sh}}{c_{sh}} < \frac{r_{sh}}{v_{sh}} < \frac{2\pi r_{sh}}{c_{sh}}. \quad (38)$$

An advective-acoustic timescale on the order of r_{sh}/v_{sh} can thus be matched by an acoustic time along an ad hoc nonradial path. This confusion between the advective and acoustic timescales could disappear if the postshock flow were very subsonic, with $\mathcal{M}_{sh} \ll (2\pi)^{-1} = 0.16$. Such conditions could be obtained in a flow involving a strong leak of energy at the shock, mimicking photodissociation in the same manner as Foglizzo et al. (2006). Unfortunately, preliminary calculations indicate that the shock distance is so much diminished by this energy loss that the $l = 1$ mode is stabilized.

We argue below that the observations of BM06 do not contradict our description of the advective-acoustic instability.

1. The resemblance between the two flows with different cooling functions (point 3) has been investigated in depth throughout this paper, showing that the instability is dominated in both flows by the advective-acoustic cycle occurring between the shock and the effective coupling radius $r_{eff} \sim r_{\nabla}$. Some significant differences were also discussed, such as the smaller frequency cutoff in the flow with $\alpha = 6$ and $\beta = 1$, which could be due to the smoother profile of the velocity gradient (Fig. 11).

2. The existence of a standing pressure wave (point 2) cannot be held against the advective-acoustic cycle, as seen in Figure 18. Most of the radial structure of the perturbed pressure shown in Figure 18 is very localized in the first 10% of the shock distance, close to the accretor, and could be compatible with Figure 7 of BM06 once projected on the $l = 1$ spherical harmonics. Let us recall that r_{eff} is an “effective” coupling radius, as defined in § 4.3, and certainly not the unique radius of acoustic emission.

3. As discussed in § 4.3, our estimate of $r_{\text{eff}} \sim r_{\nabla}$ is not accurate enough to be a decisive test for our interpretation (point 1). In a sense, our determination of r_{eff} in Figure 18 could be considered as arbitrary as the determination of an “acoustic” path in Figure 6 of BM06. Nevertheless, independent of estimating r_{eff} , we have proved the instability of the advective-acoustic cycle at high frequency in § 4 and have shown the similarity to low-frequency modes in § 5.

In view of the above detailed description of the advective-acoustic instability, together with the proven stability of the purely acoustic cycle at high frequency, the possibility that a purely acoustic mechanism may be responsible for the most unstable low-frequency modes seems unlikely.

7. CONCLUSIONS

This work is the first characterization, through a linear study, of the advective-acoustic instability in a decelerated accretion flow involving cooling processes. Our formulation of the boundary conditions at the shock corrects an error in HC92 concerning nonradial perturbations. The numerical solution of this problem confirms the existence of an $l = 1$ instability, as found in the numerical simulations of Blondin et al. (2003), for the two types of cooling functions studied by BM06. A detailed comparison of the growth time and the oscillation period of the dominant mode of the instability revealed discrepancies, which can reach $\sim 30\%$, possibly due to the numerical difficulty of advecting vorticity waves toward the region of deceleration without artificially damping them by numerical viscosity. The optimal grid size near the accretor surface is estimated as a fraction 0.1%–0.2% of the shock distance from the accretor.

The main purpose of this study was to clarify the instability mechanism at work for $l = 1$ perturbations, with the following results for both types of considered cooling functions $\alpha = 3/2$ and $\beta = 5/2$ or $\alpha = 6$ and $\beta = 1$:

1. We have proved, for the first time, that an advective-acoustic instability of the $l = 1$ mode takes place in a decelerated accretion flow involving cooling processes. The WKB approximation used in this proof required that the shock radius exceed ~ 10 times the accretor radius.

2. The low-frequency $l = 1$ instability occurring when the shock distance is moderate ($r_{\text{sh}}/r_{\nabla} \geq 2$) has also been interpreted as an advective-acoustic instability, using our conclusion 1 together with a continuity argument; the instability of the low-frequency modes can be interpreted in continuity with the instability at higher frequency in a series of flows with larger shock radii. This continuity argument is based on a comparison of both the eigenspectra (Fig. 7) and the eigenfunctions (Fig. 18) of the unstable modes.

3. The purely acoustic cycle is very stable ($|\mathcal{R}| \leq 0.5$) in the range of shock radii and frequencies allowed by our approximations. This result disfavors the acoustic interpretation of BM06.

4. The efficiency of the advective-acoustic cycle is an increasing function of the shock distance, which reaches an efficiency $|\mathcal{Q}| \sim 4$ –5 for a shock radius $r_{\text{sh}}/r_{\nabla} \sim 10$.

5. We have proposed a simple approximation of the advective-acoustic cycle timescale $\tau_{\mathcal{Q}}$ based on τ_{∇} , defined as the advection time from the shock to the radius r_{∇} where the velocity gradient is strongest, plus a radial acoustic feedback for the sake of simplicity. This estimate is quite accurate at high frequency but overestimates the cycle timescale at low frequency by $\sim 20\%$.

6. We have shown that the oscillation period of the fundamental mode is a measure of the timescale $\tau_{\mathcal{Q}}$. The oscillation period of the most unstable mode is comparable to $\tau_{\mathcal{Q}}$, $\tau_{\mathcal{Q}}/2$, or $\tau_{\mathcal{Q}}/3$ depending on the shock radius (Fig. 16).

Our efforts to understand the instability mechanism at work in a simplified flow aim at guiding our intuition when interpreting more complex numerical simulations of astrophysical flows (e.g., L. Scheck et al. 2006, in preparation). The general description of the instability is globally satisfactory, but some fundamental questions are still unanswered. The following three questions may be answered by further studies:

1. What is the maximum efficiency $|\mathcal{Q}|_{\text{max}}$ of an advective-acoustic cycle with cooling? We observed in Figure 17 that $|\mathcal{Q}|_{\text{max}}$ increases slowly with the shock distance for both types of cooling function; is this due to the influence of an extended quasi-adiabatic region where enthalpy gradients contribute to the advective-acoustic coupling (F01)? Or is this related to the cooling mechanism in the deceleration region? How does $|\mathcal{Q}|_{\text{max}}$ depend on the adiabatic index γ ? Answering these questions should help us estimate the efficiency $|\mathcal{Q}|$ in astrophysical flows with a more realistic equation of state and more elaborate cooling processes.

2. What are the conditions for the dominance of an $l = 2$ mode, as observed in Figure 6 for $\alpha = 3/2$ and $\beta = 5/2$ for $1.5 < r_{\text{sh}}/r_* < 1.9$? How does the maximum efficiency $|\mathcal{Q}|_{\text{max}}$ depend on the degree l of the perturbation? This question could be important with respect to the asymmetry of the explosion and the subsequent kick of the neutron star (Scheck et al. 2006).

3. Can we better understand the conditions under which the instability is dominated by the fundamental mode, its first harmonic, or its second harmonic? This question may be important with respect to the explosion mechanism proposed by Burrows et al. (2006). This mechanism requires the nonlinear transfer of energy from an unstable flow above the neutron star to a gravity mode of the neutron star, whose frequency can be a factor of 10 higher. We can expect that the higher the frequency of the advective-acoustic cycle, the easier the excitation of the gravity mode of the neutron star through nonlinear processes.

Some of these questions can be addressed by further simplifying the accretion flow in order to allow for analytical calculations of the advective-acoustic cycle, free from the low-frequency limitations inherent to the WKB approximation. This is the purpose of a companion paper (Foglizzo et al. 2006).

The authors are grateful to the referee, R. Chevalier, for his constructive and helpful comments. Funding by Egide (France) and by Deutscher Akademischer Austausch Dienst (DAAD; Germany) through their “Procope” exchange program and support by the Sonderforschungsbereich 375 on “Astro-Particle Physics” of the Deutsche Forschungsgemeinschaft are acknowledged. T. F. is thankful to the Kavli Institute for Theoretical Physics (KITP) for its stimulating program “The Supernovae-GRB Connection,” supported in part by the National Science Foundation under grant PHY 99-07949.

APPENDIX A

EXPLICIT RELATIONS BETWEEN δv , $\delta \rho$, δP , AND $\delta \mathcal{L}$ AND f , h , AND δK

The functions f , h , and δS can be translated into the classical variables δv_r , $\delta \rho$, δP , and δc^2 using equations (5), (7), and (8):

$$\frac{\delta v_r}{v} = \frac{1}{1 - \mathcal{M}^2} \left(h + \delta S - \frac{f}{c^2} \right), \quad (\text{A1})$$

$$\frac{\delta \rho}{\rho} = \frac{1}{1 - \mathcal{M}^2} \left(-\mathcal{M}^2 h - \delta S + \frac{f}{c^2} \right), \quad (\text{A2})$$

$$\frac{\delta P}{\gamma P} = \frac{1}{1 - \mathcal{M}^2} \left\{ -\mathcal{M}^2 h - [1 + (\gamma - 1)\mathcal{M}^2] \frac{\delta S}{\gamma} + \frac{f}{c^2} \right\}, \quad (\text{A3})$$

$$\frac{\delta c^2}{c^2} = \frac{\gamma - 1}{1 - \mathcal{M}^2} \left(\frac{f}{c^2} - \mathcal{M}^2 h - \mathcal{M}^2 \delta S \right). \quad (\text{A4})$$

The functions δK and f are related to the transverse velocity perturbation $(0, \delta v_\theta, \delta v_\varphi)$ according to the following equation, obtained from a combination of the transverse components of the Euler equation:

$$\delta A \equiv \frac{r}{\sin \theta} \left[\frac{\partial}{\partial \theta} (\sin \theta \delta v_\theta) + \frac{\partial}{\partial \varphi} \delta v_\varphi \right], \quad (\text{A5})$$

$$= \frac{1}{i\omega} [\delta K - l(l+1)f]. \quad (\text{A6})$$

Using the fact that $P = \rho c^2/\gamma$, the heating function defined by equations (1) and (4) is perturbed as follows:

$$\delta \left(\frac{\mathcal{L}}{\rho v} \right) = \nabla S \frac{c^2}{\gamma} \left[(\beta - 1) \frac{\delta \rho}{\rho} + \alpha \frac{\delta c^2}{c^2} - \frac{\delta v_z}{v} \right], \quad (\text{A7})$$

$$\delta \left(\frac{\mathcal{L}}{\rho v} \right) = \frac{\gamma}{c^2} \delta \left(\frac{\mathcal{L}}{\rho v} \right) - \frac{\delta c^2}{c^2} \nabla S. \quad (\text{A8})$$

In these equations, the perturbations δv_z , $\delta \rho$, and δc^2 can be replaced by functions of f , h , and δS using equations (A1)–(A4).

APPENDIX B

SHOCK BOUNDARY CONDITIONS

The boundary condition at the shock follows the conservation of mass flux, momentum flux, and energy flux in the frame of the shock:

$$\rho_1 (v_1 - \Delta v) = (\rho_{\text{sh}} + \delta \rho_{\text{sh}}) (v_{\text{sh}} + \delta v_{\text{sh}} - \Delta v), \quad (\text{B1})$$

$$\rho_1 (v_1 - \Delta v)^2 + \rho_1 \frac{c_1^2}{\gamma} = (\rho_{\text{sh}} + \delta \rho_{\text{sh}}) (v_{\text{sh}} + \delta v_{\text{sh}} - \Delta v)^2 + (\rho_{\text{sh}} + \delta \rho_{\text{sh}}) \frac{(c_{\text{sh}} + \delta c_{\text{sh}})^2}{\gamma}, \quad (\text{B2})$$

$$\frac{(v_1 - \Delta v)^2}{2} + \frac{c_1^2}{\gamma - 1} = \frac{(v_{\text{sh}} + \delta v_{\text{sh}} - \Delta v)^2}{2} + \frac{(c_{\text{sh}} + \delta c_{\text{sh}})^2}{\gamma - 1}, \quad (\text{B3})$$

where quantities are measured at the position $r_{\text{sh}} + \Delta \zeta$. Keeping the first-order terms and using the definitions of f and h , these equations are rewritten at the position r_{sh} using a Taylor expansion:

$$\rho_1 v_1 h_{\text{sh}} - (\rho_{\text{sh}} - \rho_1) \Delta v = \Delta \zeta \left[\frac{\partial}{\partial r} (\rho v)_1 - \frac{\partial}{\partial r} (\rho v)_{\text{sh}} \right], \quad (\text{B4})$$

$$v_{\text{sh}}^2 \delta \rho_{\text{sh}} + 2 \rho_{\text{sh}} v_{\text{sh}} \delta v_{\text{sh}} + \frac{2}{\gamma} \rho_{\text{sh}} c_{\text{sh}} \delta c_{\text{sh}} + \delta \rho_{\text{sh}} \frac{c_{\text{sh}}^2}{\gamma} = \Delta \zeta \left[\frac{\partial}{\partial r} (\rho v^2 + P)_1 - \frac{\partial}{\partial r} (\rho v^2 + P)_{\text{sh}} \right], \quad (\text{B5})$$

$$f_{\text{sh}} - (v_{\text{sh}} - v_1) \Delta v = \Delta \zeta \left[\frac{\partial}{\partial r} \left(\frac{v^2}{2} + \frac{c^2}{\gamma - 1} \right)_1 - \frac{\partial}{\partial r} \left(\frac{v^2}{2} + \frac{c^2}{\gamma - 1} \right)_{\text{sh}} \right]. \quad (\text{B6})$$

From equations (2), (3), and (4) of the stationary flow,

$$\frac{\partial}{\partial r}(\rho v) = -2 \frac{\rho v}{r}, \quad (\text{B7})$$

$$\frac{\partial}{\partial r}(P + \rho v^2) = -\rho \frac{GM}{r^2} - 2 \frac{\rho v^2}{r}, \quad (\text{B8})$$

$$\frac{\partial}{\partial r}\left(\frac{v^2}{2} + \frac{c^2}{\gamma - 1}\right) = \frac{\mathcal{L}}{\rho v} - \frac{GM}{r^2}. \quad (\text{B9})$$

We obtain

$$h_{\text{sh}} = \left(\frac{1}{v_{\text{sh}}} - \frac{1}{v_1}\right) \Delta v, \quad (\text{B10})$$

$$\frac{\delta S_{\text{sh}}}{\gamma} = \frac{\Delta \zeta}{c_{\text{sh}}^2} \left[\frac{\mathcal{L}_1}{\rho_1 v_1} - \frac{\mathcal{L}_{\text{sh}}}{\rho_{\text{sh}} v_{\text{sh}}} - \left(\frac{GM}{r_{\text{sh}}^2} - 2 \frac{v_1 v_{\text{sh}}}{r_{\text{sh}}} \right) \left(1 - \frac{v_{\text{sh}}}{v_1} \right) \right] - \frac{v_1 \Delta v}{c_{\text{sh}}^2} \left(1 - \frac{v_{\text{sh}}}{v_1} \right)^2, \quad (\text{B11})$$

$$f_{\text{sh}} = (v_{\text{sh}} - v_1) \Delta v + \Delta \zeta \left(\frac{\mathcal{L}_1}{\rho_1 v_1} - \frac{\mathcal{L}_{\text{sh}}}{\rho_{\text{sh}} v_{\text{sh}}} \right). \quad (\text{B12})$$

In the entropy equation, the gravity term GM/r_{sh}^2 and the term $v_1 v_{\text{sh}}/r_{\text{sh}}$ due to the spherical geometry can be rewritten as

$$\frac{GM}{r_{\text{sh}}^2} - 2 \frac{v_1 v_{\text{sh}}}{r_{\text{sh}}} = \frac{v_{\text{ff}}^2}{2r_{\text{sh}}} - 2 \frac{v_1 v_{\text{sh}}}{r_{\text{sh}}} \quad (\text{B13})$$

$$= \frac{v_1^2}{2r_{\text{sh}}} \left[\left(\frac{v_{\text{ff}}}{v_1} \right)^2 - 4 \frac{v_{\text{sh}}}{v_1} \right]. \quad (\text{B14})$$

The transverse velocity immediately after the shock is deduced from the conservation of the tangential component of the velocity, in the spirit of Landau & Lifschitz (1989), leading to equations (22) and (23). The variable δA_{sh} is deduced from its definition (A5) and equations (22) and (23):

$$\delta A_{\text{sh}} = -l(l+1)(v_1 - v_{\text{sh}}) \Delta \zeta. \quad (\text{B15})$$

The variable δK_{sh} is deduced from δA_{sh} using equations (A6) and (B12). The assumption that $\mathcal{L}_1 \ll \mathcal{L}_{\text{sh}}$, with $\mathcal{L}_{\text{sh}} = \rho_{\text{sh}} v_{\text{sh}} c_{\text{sh}}^2 \nabla S_{\text{sh}}/\gamma$, leads to equations (15), (16), and (17) if the shock is strong.

APPENDIX C

PROJECTION OF PERTURBATIONS ON ACOUSTIC AND ADVECTED WAVES

C1. UNIFORM ADIABATIC FLOW

In a uniform, adiabatic flow moving at constant velocity in the direction z , any perturbation f , h , δS , or δK associated with the frequency ω and perpendicular wavenumber k_{\perp} can be decomposed into a sum of acoustic waves and advected waves as

$$f = f^+ + f^- + f^S + f^K, \quad (\text{C1})$$

$$h = h^+ + h^- + h^S + h^K, \quad (\text{C2})$$

where an acoustic wave is denoted by f^+ or h^+ if it propagates in the direction of the flow, and f^- or h^- otherwise. The contribution to f and h of a vorticity perturbation δK such that $\delta S = 0$ is

$$f^K = \frac{\mathcal{M}^2(1 - \mu^2)}{1 - \mu^2 \mathcal{M}^2} \frac{\delta K}{k_{\perp}^2}, \quad (\text{C3})$$

$$h^K = \frac{f^K}{v^2}, \quad (\text{C4})$$

where $\mu^2 \equiv 1 - k_{\perp}^2 c^2 (1 - \mathcal{M}^2)/\omega^2$. An entropy-vorticity perturbation such that $\delta K = 0$ contributes to the perturbation f and h as follows:

$$\frac{f^S}{c^2} = \frac{1 - \mathcal{M}^2}{1 - \mu^2 \mathcal{M}^2} \frac{\delta S}{\gamma}, \quad (\text{C5})$$

$$h^S = \frac{\mu^2}{c^2} f^S - \delta S. \quad (\text{C6})$$

The acoustic component in a uniform adiabatic flow is deduced from f , h , δS , and δK through

$$f^\pm = \frac{1}{2}f \pm \frac{\mathcal{M}c^2}{2\mu}(h + \delta S) - \frac{1 \pm \mu\mathcal{M}}{2} \left(f^S \pm \frac{f_K}{\mu\mathcal{M}} \right), \quad (C7)$$

$$h^\pm = \pm \frac{\mu}{\mathcal{M}} \frac{f^\pm}{c^2}. \quad (C8)$$

C2. EXTENSION TO A SPHERICAL FLOW WITH COOLING

In a spherical flow with gradients, the advected and propagating waves are no longer independent but coupled, even if the flow is adiabatic. Moreover, cooling processes are responsible for an additional coupling between advected and propagating perturbations. We choose to use the same decomposition obtained in a uniform adiabatic flow, adapted to spherical coordinates by replacing μ^2 by the spherical value (eq. [14]), and k_\perp^2 by $l(l+1)/r^2$ (the eigenvalue of the Laplacian operator):

$$f^K \equiv \frac{\mathcal{M}^2(1-\mu^2)}{1-\mu^2\mathcal{M}^2} \frac{\delta K}{l(l+1)}, \quad (C9)$$

$$h^K \equiv \frac{f^K}{v^2}, \quad (C10)$$

$$\frac{f^S}{c^2} \equiv \frac{1-\mathcal{M}^2}{1-\mu^2\mathcal{M}^2} \frac{\delta S}{\gamma}, \quad (C11)$$

$$h^S \equiv \frac{\mu^2}{c^2} f^S - \delta S. \quad (C12)$$

$$f^\pm \equiv \frac{1}{2}f \pm \frac{\mathcal{M}c^2}{2\mu}(h + \delta S) - \frac{1 \pm \mu\mathcal{M}}{2} \left(f^S \pm \frac{f_K}{\mu\mathcal{M}} \right), \quad (C13)$$

$$h^\pm \equiv \pm \frac{\mu}{\mathcal{M}} \frac{f^\pm}{c^2}. \quad (C14)$$

For any perturbation f , h , δS , or δK in a spherical nonadiabatic flow, the quantities (f^\pm, f^K, f^S) and (h^\pm, h^K, h^S) defined above naturally satisfy

$$f = f^+ + f^- + f^S + f^K, \quad (C15)$$

$$h = h^+ + h^- + h^S + h^K. \quad (C16)$$

This decomposition describes the amount of advected and propagating waves that would be measured if the perturbation were allowed to continue its evolution in a uniform adiabatic flow. We choose to apply this decomposition at the shock radius on the subsonic side. The identification of f^\pm with acoustic waves is strictly valid in the WKB approximation when the wavelength is short compared to the scale of the gradients in the flow. The threshold of validity of this approximation is evaluated in § 4.2.4.

APPENDIX D

NUMERICAL PROCEDURE TO CALCULATE \mathcal{R}_∇ , \mathcal{Q}_∇ , AND \mathcal{Q}_∇^K

One consequence of cooling is the fact that vorticity and entropy perturbations produced at the shock do not satisfy $\delta K_{\text{sh}} \equiv 0$ as in adiabatic flows (eq. [18]). This raises the question of the acoustic feedback produced by the advection of the residual value of δK_{sh} generated by cooling at the shock. The global efficiency \mathcal{Q}^K associated with this feedback is thus also computed as a check of consistency; this feedback is indeed small in all our calculations ($|\mathcal{Q}^K| < 0.1$).

D1. NUMERICAL CALCULATION OF \mathcal{R}_∇ , \mathcal{Q}_∇ , AND \mathcal{Q}_∇^K

For a given frequency ω_r and degree l , the differential system is integrated four times from r_{sh} to r_* with the following boundary conditions:

1. Acoustic wave propagating downward:

$$\delta K_{\text{sh}} = 0, \quad \delta S_{\text{sh}} = 0, \quad f_{\text{sh}} = f_{\text{sh}}^+ = 1, \quad h_{\text{sh}} = \frac{\mu_{\text{sh}}}{\mathcal{M}_{\text{sh}}} \frac{f_{\text{sh}}}{c_{\text{sh}}^2}. \quad (D1)$$

2. Acoustic wave propagating upward:

$$\delta K_{\text{sh}} = 0, \quad \delta S_{\text{sh}} = 0, \quad f_{\text{sh}} = f_{\text{sh}}^- = 1, \quad h_{\text{sh}} = -\frac{\mu_{\text{sh}}}{\mathcal{M}_{\text{sh}}} \frac{f_{\text{sh}}}{c_{\text{sh}}^2}. \quad (D2)$$

3. Entropy/vorticity wave advected downward:

$$\delta K_{\text{sh}} = 0, \quad \delta S_{\text{sh}} = 1, \quad f_{\text{sh}} = f_{\text{sh}}^S, \quad h_{\text{sh}} = h_{\text{sh}}^S. \quad (\text{D3})$$

4. Vorticity wave advected downward:

$$\delta K_{\text{sh}} = 1, \quad \delta S_{\text{sh}} = 0, \quad f_{\text{sh}} = f_{\text{sh}}^K, \quad h_{\text{sh}} = h_{\text{sh}}^K. \quad (\text{D4})$$

In each of these four cases, the differential system is integrated from the shock down to the accretor surface r_* , where the velocity perturbation reaches a value $(\delta v/v)(r_*)$ denoted by a_+ , a_- , a_S , and a_K , respectively. A linear combination of a couple of these integrated solutions allows us to construct three solutions, which fulfill the boundary condition $(\delta v/v)(r_*) = 0$, and measure at the shock radius the following efficiencies of acoustic feedback within the flow:

1. Acoustic reflection, without any advected perturbation at the shock:

$$\mathcal{R}_{\nabla} \equiv -\frac{a_+}{a_-}. \quad (\text{D5})$$

2. Acoustic feedback produced by an entropy/vorticity perturbation such that $\delta K_{\text{sh}} = 0$:

$$\mathcal{Q}_{\nabla} \equiv -\frac{1}{a_-} \frac{a_S}{f^S}. \quad (\text{D6})$$

3. Acoustic feedback produced by a vorticity perturbation such that $\delta S_{\text{sh}} = 0$:

$$\mathcal{Q}_{\nabla}^K \equiv -\frac{1}{a_-} \frac{a_K}{f^K}. \quad (\text{D7})$$

D2. CALCULATION OF \mathcal{R}_{sh} , \mathcal{Q}_{sh} , AND $\mathcal{Q}_{\text{sh}}^K$

At the shock, the coupling coefficients \mathcal{R}_{sh} , \mathcal{Q}_{sh} , and $\mathcal{Q}_{\text{sh}}^K$ are defined by

$$\mathcal{R}_{\text{sh}} \equiv \frac{f_{\text{sh}}^+}{f_{\text{sh}}^-}, \quad (\text{D8})$$

$$\mathcal{Q}_{\text{sh}} \equiv \frac{f_{\text{sh}}^S}{f_{\text{sh}}^-}, \quad (\text{D9})$$

$$\mathcal{Q}_{\text{sh}}^K \equiv \frac{f_{\text{sh}}^K}{f_{\text{sh}}^-}, \quad (\text{D10})$$

where f_{sh}^{\pm} , f_{sh}^S , and f_{sh}^K are deduced from equations (C3), (C5), and (C7), with the boundary values f_{sh} , h_{sh} , δS_{sh} , and δK_{sh} established in equations (15)–(18). Although cooling is neglected in the projection of the perturbation f on f^{\pm} , f^K , and f^S (eqs. [C9]–[C14]), some effect of cooling on the jump conditions is taken into account through f_{sh}^{\pm} , f_{sh}^S , and f_{sh}^K .

REFERENCES

- Abouseif, G. E., Keklak, J. A., & Toong, T. Y. 1984, *Combustion Sci. Tech.*, 36, 83
- Bertschinger, E. 1986, *ApJ*, 304, 154
- Blondin, J. M., & Mezzacappa, A. 2006, *ApJ*, 642, 401 (BM06)
- Blondin, J. M., Mezzacappa, A., & DeMarino, C. 2003, *ApJ*, 584, 971
- Burrows, A., Livne, E., Dessart, L., Ott, C. D., & Murphy, J. 2006, *ApJ*, 640, 878
- Candel, S. M. 1972, Ph.D. thesis, California Inst. of Tech.
- Chevalier, R. A., & Imamura, J. N. 1982, *ApJ*, 261, 543
- Foglizzo, T. 2001, *A&A*, 368, 311 (F01)
- . 2002, *A&A*, 392, 353 (F02)
- Foglizzo, T., & Galletti, P. 2003, in *Proc. Cosmic Explosions in Three Dimensions*, ed. P. Hoflich, P. Kumar, & J. C. Wheeler (Cambridge: Cambridge Univ. Press), 238
- Foglizzo, T., Galletti, P., & Ruffert, M. 2005, *A&A*, 435, 397
- Foglizzo, T., Scheck, L., & Janka, H. T. 2006, *ApJ*, 652, 1436
- Foglizzo, T., & Tagger, M. 2000, *A&A*, 363, 174
- Houck, J. C., & Chevalier, R. A. 1992, *ApJ*, 395, 592 (HC92)
- Howe, M. S. 1975, *J. Fluid Mech.*, 71, 625
- Imamura, J. N., Aboasha, A., Wolff, M. T., & Wood, K. S. 1996, *ApJ*, 458, 327
- Janka, H. T., Scheck, L., Kifonidis, K., Müller, E., & Plewa, T. 2004, in *ASP Conf. Ser. 332, The Fate of the Most Massive Stars*, ed. R. Humphreys & K. Stanek (San Francisco: ASP), 372
- Landau, L., & Lifschitz, E. 1989, *Fluid Mechanics* (2nd ed.; New York: Pergamon)
- Marble, F. E., & Candel, S. M. 1977, *J. Sound Vibration*, 55, 225
- Ohnishi, N., Kotake, K., & Yamada, S. 2006, *ApJ*, 641, 1018
- Saxton, C. J. 2002, *Publ. Astron. Soc. Australia*, 19, 282
- Saxton, C. J., & Wu, K. 1999, *MNRAS*, 310, 677
- Scheck, L., Kifonidis, K., Janka, H. T., & Müller, E. 2006, *A&A*, 457, 963
- Scheck, L., Plewa, T., Janka, H.-T., & Müller, E. 2004, *Phys. Rev. Lett.*, 92, 1103